REGULATION OF SUPERCOOLED LIQUID SULFUR IN LITHIUM-SULFUR BATTERIES

by

YUE ZHANG

A thesis submitted in partial fulfillment of the
requirements for the degree of

MASTER OF SCIENCE IN MECHANICAL ENGINEERING

2026

Oakland University
Rochester, Michigan

Thesis Advisory Committee:

Ankun Yang, Ph.D., Chair
Xia Wang, Ph.D.
Hongwei Qu, Ph.D.

To my mother and father

ACKNOWLEDGEMENTS

I would like to express my sincere gratitude to my advisor, Dr. Ankun Yang, for his guidance, encouragement, and continuous support throughout my master's study and this research. His expertise and patience have greatly contributed to the completion of this thesis.

I would also like to thank my thesis committee members, Dr. Xia Wang and Dr. Hongwei Qu, for their valuable comments and suggestions, which helped improve the quality of this work.

My appreciation is extended to all members of the Yang Research Group for their assistance, discussions, and support during my research.

Finally, I would like to thank my family for their unconditional love, encouragement, and support throughout my academic journey.

Yue Zhang

ABSTRACT

REGULATION OF SUPERCOOLED LIQUID SULFUR IN LITHIUM-SULFUR BATTERIES

by

Yue Zhang

Adviser: Ankun Yang, Ph.D.

Lithium–sulfur batteries offer high theoretical energy density but remain limited by complex sulfur-conversion reactions and uncontrolled sulfur redistribution. This thesis investigates how electrolyte additives regulate the formation and evolution of supercooled liquid sulfur using a customized in situ optical electrochemical cell. Two mediator systems were examined: lithium iodide (LiI) and reduced isopropylxanthic disulfide (DIP-Red). In the baseline LiTFSI electrolyte, sulfur droplets formed mainly on or near the Pt wire. Adding LiI caused earlier droplet formation, higher visible droplet density, and broader sulfur distribution, supporting an iodine-mediated polysulfide-oxidation pathway. In contrast, DIP-Red did not generate sulfur throughout the electrolyte but promoted post-nucleation droplet growth, displacement, detachment, and redistribution. Raman spectroscopy confirmed that the observed droplets contained elemental sulfur. These results demonstrate that LiI and DIP-Red regulate supercooled liquid sulfur through distinct mechanisms and highlight the value of direct optical visualization for studying dynamic sulfur-conversion processes.

TABLE OF CONTENTS

TABLE OF CONTENTS—Continued

TABLE OF CONTENTS—Continued

LIST OF FIGURES

LIST OF ABBREVIATIONS

AB	Epoxy Adhesive
DIP	Isopropylxanthic Disulfide
DIP-Red	Reduced Isopropylxanthic Disulfide
DME	1,2-Dimethoxyethane
DOL	1,3-Dioxolane
LIB	Lithium-Ion Battery
Li-S	Lithium–Sulfur
LiI	Lithium Iodide
$LiNO_3$	Lithium Nitrate
LiTFSI	Lithium Bis(trifluoromethanesulfonyl)imide
PS	Lithium Polysulfide
Pt	Platinum
SiO_2	Silicon Dioxide

CHAPTER ONE

INTRODUCTION

1.1 Background and Motivation

The rapid growth of portable electronics, electric vehicles, and large-scale renewable-energy systems has increased the demand for advanced electrochemical energy-storage technologies (Goodenough & Park, 2013; Manthiram, 2020). Lithium-ion batteries (LIBs) have dominated the rechargeable-battery market because of their high energy density, long cycle life, and mature manufacturing technology. Conventional LIBs commonly use graphite anodes and layered transition-metal oxide cathodes, with energy stored through reversible lithium-ion intercalation reactions. These characteristics have enabled their widespread use in consumer electronics, electric transportation, and stationary energy-storage systems.

Despite their commercial success, conventional LIBs are approaching the practical limits of their energy density (Goodenough & Park, 2013). Applications such as long-range electric vehicles and grid-scale storage require battery systems that can provide higher energy density while maintaining reasonable cost, safety, and cycle life. In addition, the use of critical elements such as cobalt and nickel raises concerns related to material cost, resource availability, and long-term sustainability. These limitations have motivated the development of rechargeable battery chemistries beyond conventional lithium-ion systems (Whittingham, 2012).

Among the proposed next-generation technologies, lithium–sulfur (Li–S) batteries have attracted substantial attention because sulfur has a theoretical specific capacity of 1675

mAh g^{-1} and a theoretical energy density approaching 2600 Wh kg^{-1}. These values are considerably higher than those of conventional lithium-ion cathode materials. Sulfur is also naturally abundant, inexpensive, and relatively environmentally benign, making Li–S batteries promising candidates for future high-energy-density storage applications (Manthiram et al., 2014; Seh et al., 2016; Pang et al., 2016).

The practical application of Li–S batteries, however, remains limited due to the complexity of sulfur conversion. During discharge, elemental sulfur is reduced through a series of soluble lithium polysulfide intermediates before forming insoluble lithium sulfide (Li_2S). During charging, the reverse reactions regenerate elemental sulfur. The dissolution and transport of lithium polysulfides produce the well-known shuttle effect, which contributes to active-material loss, low Coulombic efficiency, capacity fading, and poor cycling stability. In addition, the low electronic conductivity of both sulfur and Li_2S leads to sluggish reaction kinetics and incomplete active-material utilization (Manthiram et al., 2014; Seh et al., 2016).

Sulfur regenerated during charging has traditionally been described as precipitating directly in the form of crystalline solid sulfur. Recent in situ optical studies have shown that this description is incomplete (Liu et al., 2019; Subramaniam-Venkatesh et al., 2025). Under appropriate electrochemical conditions, sulfur can initially form as metastable liquid droplets at ambient temperature. Because these droplets remain liquid below the equilibrium melting temperature of sulfur, they are referred to as supercooled liquid sulfur (Subramaniam-Venkatesh et al., 2025).

Supercooled liquid sulfur exhibits dynamic behaviors that are not characteristic of rigid solid particles. These behaviors include droplet nucleation, growth, coalescence,

migration, displacement, and detachment from the electrode surface. Such processes can influence sulfur transport, redistribution, and interfacial reaction behavior during charging. Therefore, understanding the formation and evolution of supercooled liquid sulfur is important for developing a more complete description of sulfur-conversion mechanisms in Li–S batteries (Subramaniam-Venkatesh et al., 2025).

Electrolyte engineering provides an effective approach for regulating sulfur chemistry. Functional additives and redox mediators can alter sulfur-conversion pathways, modify reaction kinetics, and influence the transport and distribution of sulfur-containing species (Seh et al., 2016; Pang et al., 2016). However, the effect of different electrolyte additives on supercooled liquid sulfur formation remains insufficiently understood.

1.2 Electrochemistry of Lithium–Sulfur Batteries

Lithium–sulfur batteries operate through multistep conversion reactions involving elemental sulfur and lithium sulfide rather than the lithium-ion intercalation mechanism employed in conventional lithium-ion batteries. Owing to these fundamentally different reaction mechanisms, Li–S batteries exhibit much higher theoretical energy density but also significantly more complicated electrochemical behavior (Seh et al., 2016).

A typical lithium–sulfur battery consists of a lithium metal anode, a sulfur-based cathode, a porous separator, and an ether-based electrolyte. During discharge, elemental sulfur accepts electrons and reacts with lithium ions to form a series of soluble lithium polysulfides before finally producing insoluble lithium sulfide. During charging, these reactions proceed in the reverse direction and regenerate elemental sulfur (Manthiram et al., 2014).

The sulfur-conversion reactions can be generally expressed as

$$S_8 \rightleftharpoons Li_2S_8 \rightleftharpoons Li_2S_6 \rightleftharpoons Li_2S_4 \rightleftharpoons Li_2S_2 \rightleftharpoons Li_2S$$

As illustrated in Figure 1.1, the discharge profile of a typical Li–S battery is generally divided into two voltage plateaus, which originate from the stepwise reduction of elemental sulfur. During the upper plateau, $S_8$is reduced to soluble long-chain lithium polysulfides, including Li_2S_8, Li_2S_6, and Li_2S_4. These soluble intermediates contribute significantly to the discharge capacity, but they can also diffuse into the electrolyte and cause the polysulfide shuttle effect. During the lower plateau, long-chain polysulfides are further reduced to short-chain polysulfides and eventually form insoluble$Li_2S_2$and Li_2S, which precipitate on the cathode surface. The formation of these insulating solid products can slow sulfur redox kinetics and reduce active-material utilization (Manthiram et al., 2014; Seh et al., 2016).

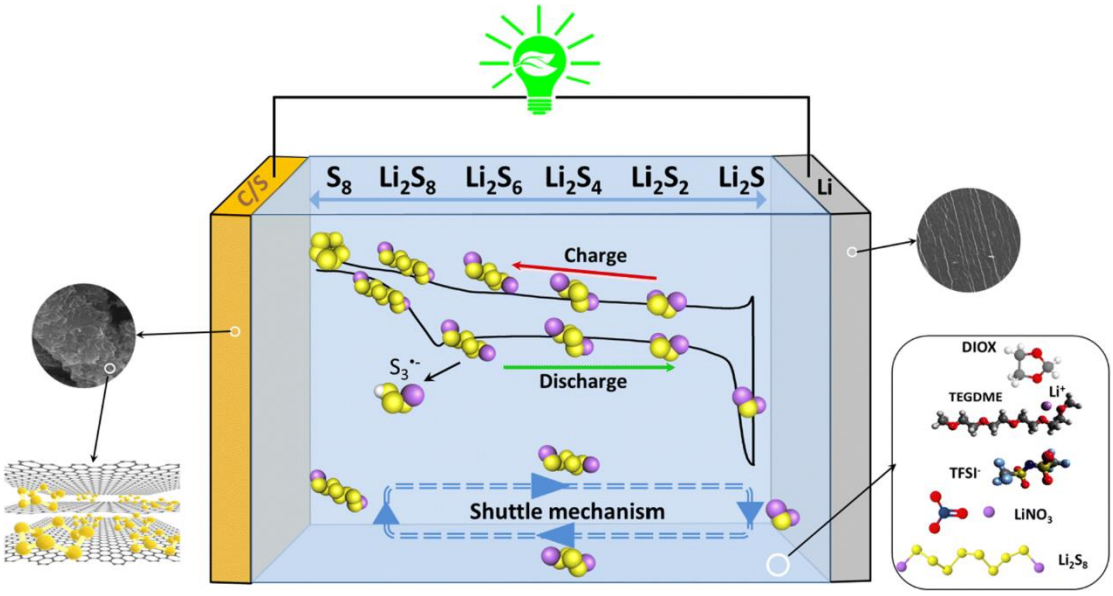

Figure 1.1 Schematic illustration of the charge–discharge reactions and polysulfide shuttle mechanism in a conventional lithium–sulfur battery. Adapted from Xiong et al. (2018).

During discharge, elemental sulfur is reduced through soluble long-chain lithium polysulfides and eventually forms insoluble Li_2S_2 and Li_2S. During charging, the reverse oxidation process regenerates sulfur. The dissolution and migration of polysulfides between the cathode and lithium anode lead to the shuttle effect. During charging, Li_2S undergoes electrochemical oxidation and is gradually converted back into elemental sulfur through the reverse sequence. Unlike insertion-type electrodes, sulfur conversion involves continuous phase transitions among dissolved, liquid, and solid sulfur species. Consequently, sulfur-conversion behavior is strongly influenced by electrolyte composition, sulfur concentration, interfacial reactions, and mass transport (Pang et al., 2016).

Several challenges limit the practical application of lithium–sulfur batteries. First, elemental sulfur and the final discharge products, $Li_2S_2$and Li_2S, are electronically insulating. Their poor conductivity limits electron transport during sulfur conversion, so electrochemical reactions can only proceed efficiently at conductive interfaces. This results in sluggish reaction kinetics, incomplete conversion, and low active-material utilization.

Second, soluble lithium polysulfides cause the polysulfide shuttle effect. During discharge, long-chain polysulfides dissolve into the ether-based electrolyte and diffuse from the cathode toward the lithium metal anode. At the anode, they can be chemically reduced to shorter-chain species or insoluble Li_2S_2/Li_2S. These reduced species may diffuse back to the cathode and become re-oxidized during charging, forming a

continuous shuttle process. This repeated migration causes active-material loss, electrolyte consumption, low Coulombic efficiency, and rapid capacity fading.

In addition, reactions between polysulfides and the lithium metal anode destabilize the solid–electrolyte interphase and promote nonuniform lithium deposition. The resulting dendrite growth increases safety risks and further accelerates cell degradation. Therefore, poor electronic conductivity, polysulfide shuttling, and lithium-anode instability are closely coupled challenges in Li–S batteries (Manthiram et al., 2014; Seh et al., 2016; Pang et al., 2016).

Recent in situ optical studies have revealed that sulfur evolution during charging differs substantially from the conventional solid-precipitation model. Instead of directly forming crystalline sulfur, electrochemically generated sulfur can first appear as supercooled liquid droplets that remain metastable under ambient conditions (Liu et al., 2019; Shi et al., 2023). These droplets undergo nucleation, growth, coalescence, migration, detachment, and redistribution before eventual solidification, indicating that sulfur conversion involves both electrochemical reactions and dynamic phase evolution. More recently, chemically generated liquid sulfur droplets were also observed when redox mediators oxidized polysulfides in the electrolyte, demonstrating that liquid sulfur can form close to but away from the electrode surface (Subramaniam-Venkatesh et al., 2025). This finding provides the central motivation for this thesis: if sulfur passes through a liquid-droplet intermediate state, then electrolyte mediators may regulate sulfur conversion by changing the location, morphology, and dynamics of sulfur formation. Accordingly, this work investigates how LiI and DIP-Red influence supercooled liquid sulfur evolution using real-time in situ optical observation.

1.3 Supercooled Liquid Sulfur Formation in Lithium–Sulfur Batteries

For many years, sulfur regeneration during the charging process of lithium–sulfur batteries have been interpreted using the conventional solid-precipitation model, in which elemental sulfur is assumed to nucleate and grow directly as crystalline particles after the oxidation of lithium sulfide. This assumption is mainly based on the fact that elemental sulfur has a melting temperature of approximately 115 °C under ambient pressure and therefore should exist as a solid phase during normal battery operation.

Recent advances in in situ optical visualization, however, have revealed that sulfur evolution is considerably more complicated than this traditional description. Instead of immediately forming solid sulfur particles, electrochemically generated sulfur can initially appear as discrete liquid droplets that remain stable at room temperature, well below the equilibrium melting temperature of sulfur (Liu et al., 2019). Because these droplets exist below the melting temperature of sulfur, they are referred to as supercooled liquid sulfur. More recent studies further showed that redox mediators can chemically oxidize dissolved polysulfides and generate liquid sulfur droplets in the electrolyte, close to but away from the electrode surface (Subramaniam-Venkatesh et al., 2025).

These findings indicate that sulfur regeneration during charging is not simply a solid-precipitation process, but a dynamic phase-evolution process involving the formation, growth, motion, and eventual solidification of liquid sulfur droplets. This understanding provides the motivation for the present thesis, which investigates how electrolyte mediators such as LiI and DIP-Red regulate the location, morphology, and evolution of supercooled liquid sulfur during sulfur oxidation.

Unlike solid sulfur particles, supercooled liquid sulfur exhibits highly dynamic behavior throughout the charging process. After the initial formation of sulfur droplets, continuous sulfur oxidation supplies additional sulfur species to the liquid phase, resulting in progressive droplet growth. As neighboring droplets come into contact, they readily merge into larger droplets through coalescence, followed by rapid relaxation toward spherical morphologies due to surface tension. In addition, sulfur droplets are capable of migrating along the electrode surface or detaching from the electrode into the surrounding electrolyte, indicating that sulfur transport involves liquid-phase motion rather than conventional solid-state diffusion.

These dynamic behaviors cannot be explained by traditional sulfur precipitation models and suggest that sulfur evolution proceeds through an intermediate liquid phase before final solidification. Consequently, sulfur conversion in lithium-sulfur batteries should be regarded as a coupled electrochemical and physicochemical process involving sulfur generation, liquid-phase transport, droplet interaction, and eventual solidification.

The formation of supercooled liquid sulfur is influenced by several factors, including sulfur concentration, electrolyte composition, interfacial properties, electrochemical conditions, and sulfur transport within the electrolyte. Changes in electrolyte chemistry may significantly alter sulfur evolution behavior by modifying sulfur conversion kinetics, sulfur solubility, or sulfur transport pathways. Therefore, regulating sulfur evolution through electrolyte engineering provides an effective strategy for controlling sulfur morphology and improving sulfur utilization.

Direct visualization of supercooled liquid sulfur also provides information that cannot be obtained from conventional electrochemical measurements. While voltage profiles and

electrochemical performance reflect the overall reaction behavior, they cannot directly reveal where sulfur forms, how sulfur droplets evolve, or how sulfur is redistributed during electrochemical cycling. Consequently, in situ optical visualization has become an important experimental technique for investigating sulfur-conversion mechanisms and understanding the relationship between electrolyte composition and sulfur evolution.

1.4 Strategies for Regulating Sulfur Conversion

Because sulfur conversion involves multiple dissolved, liquid, and solid sulfur-containing species, electrolyte engineering has become one of the most effective approaches for regulating sulfur chemistry in lithium–sulfur batteries. By adjusting the electrolyte solvent, salt concentration, additive composition, and redox-mediator chemistry, the sulfur-conversion pathway can be modified without changing the overall cell architecture. These strategies can improve sulfur utilization by accelerating sulfur redox reactions, suppressing undesirable side reactions, limiting polysulfide shuttling, and regulating sulfur transport and deposition behavior (Seh et al., 2016; Pang et al., 2016). Among different electrolyte-engineering strategies, redox mediators and functional organic additives have attracted increasing attention because they can directly participate in sulfur-conversion reactions. These additives provide additional chemical or electrochemical pathways for converting lithium polysulfides, thereby reducing reaction barriers and improving the reversibility of sulfur redox chemistry. In particular, redox mediators are useful for modifying the oxidation of lithium polysulfides during charging, where sulfur regeneration and sulfur morphology strongly depend on the local reaction environment (Liang et al., 2015; Gerber et al., 2016; Pang et al., 2016).

1.4.1 Lithium Iodide as a Redox Mediator

Lithium iodide (LiI) has been widely investigated as an inorganic redox mediator for lithium–sulfur batteries. During charging, iodide ions can be electrochemically oxidized at the cathode or working-electrode surface to generate iodine-containing species. These oxidized iodine species can then diffuse into the electrolyte and chemically oxidize dissolved lithium polysulfides back to elemental sulfur, while being reduced to iodide. Through this redox-mediation cycle, LiI can promote polysulfide oxidation, reduce polarization during sulfur regeneration, and improve the reversibility of sulfur conversion (Liang et al., 2015; Pang et al., 2016).

In addition to affecting sulfur-conversion kinetics, LiI can also influence the spatial distribution of sulfur formation. Recent optical studies have shown that redox-mediated chemical oxidation can generate liquid sulfur droplets in the electrolyte, including regions away from the immediate electrode surface (Subramaniam-Venkatesh et al., 2025). This behavior suggests that iodine-mediated polysulfide oxidation may provide an additional sulfur-generation pathway beyond direct electrochemical oxidation at the electrode/electrolyte interface. As a result, sulfur formation can become less localized near the electrode and more broadly distributed within the electrolyte.

Although LiI has been used to improve sulfur utilization and cycling stability, the effect of LiI concentration on the formation and evolution of supercooled liquid sulfur has not been systematically visualized. In particular, it remains unclear how increasing LiI concentration changes the onset of visible sulfur droplets, the spatial extent of sulfur generation, and the morphology of sulfur droplets during charging. Direct in situ optical observation therefore provides an opportunity to examine how LiI concentration regulates sulfur morphology and sulfur-evolution behavior during electrochemical oxidation.

1.4.2 Isopropylxanthic Disulfide as an Organic Sulfur-Conversion Mediator

Organic sulfur-conversion mediators have recently emerged as another promising electrolyte-engineering strategy for lithium-sulfur batteries. Compared with conventional inorganic redox mediators, organic molecules provide greater structural flexibility and may participate in sulfur chemistry through reversible redox reactions and chemical interactions with dissolved polysulfides.

Among these materials, isopropylxanthic disulfide (DIP) has recently attracted attention as an organic sulfur-conversion mediator. Previous studies have shown that DIP can be reduced through cleavage of its redox-active S–S bond to form DIP-derived reduced species, referred to as DIP-Red. These reduced species can interact with lithium polysulfides and facilitate charge transfer during sulfur redox reactions (Zhang et al., 2026). Rather than directly generating sulfur, DIP primarily functions as a molecular mediator that regulates polysulfide conversion and sulfur evolution. Although the electrochemical role of DIP has been reported, its influence on sulfur morphology and supercooled liquid sulfur evolution remains largely unknown. Direct observation of sulfur evolution in DIP-containing electrolytes therefore provides an opportunity to establish the relationship between sulfur-conversion mediation and sulfur morphology. Understanding these processes will contribute to the development of more effective electrolyte additives for advanced lithium-sulfur batteries.

1.5 Objectives and Scope

The primary objective of this thesis is to directly visualize the formation and evolution of supercooled liquid sulfur during sulfur oxidation and to understand how electrolyte additives regulate sulfur-conversion behavior in Li–S batteries.

To achieve this objective, a customized in situ optical electrochemical cell was used as the main experimental platform. This platform allowed sulfur droplet nucleation, growth, coalescence, migration, detachment, and redistribution to be observed in real time under a designed electrochemical potential or current controlled by a potentiostat. The optical observations were combined with electrochemical measurements and Raman spectroscopy to evaluate sulfur morphology, phase identity, and sulfur-evolution behavior.

The first part of this work focuses on lithium iodide (LiI), a known inorganic redox mediator. A series of LiI-containing electrolytes was prepared to investigate the effect of LiI concentration on supercooled liquid sulfur formation. The study examines how LiI concentration influences the onset of visible sulfur droplets, droplet density, spatial distribution, and current–time transients during potentiostatic oxidation. This part aims to clarify how iodine-mediated polysulfide oxidation chemically generates sulfur in the electrolyte and changes where sulfur forms relative to the Pt wire.

The second part of this work investigates isopropylxanthic disulfide (DIP) and its reduced form, DIP-Red, as an organic sulfur-conversion mediator system. DIP-Red preparation was first optimized by comparing sulfur sources and DIP-to-Li_2S molar ratios. The optimized DIP-Red electrolyte was then used to examine sulfur droplet evolution in glyme-based systems. Particular attention was given to droplet growth, displacement, detachment, and redistribution after nucleation on the Pt wire. This part aims to evaluate how DIP-derived species regulate sulfur evolution through molecular mediation and interaction with lithium polysulfide species.

Through these investigations, this thesis compares two distinct electrolyte-mediator strategies for regulating supercooled liquid sulfur. LiI is used as a known iodine-mediated chemical sulfur-generation system, while DIP-Red is explored as an organic mediator that modifies post-nucleation droplet evolution. Together, these studies provide direct optical evidence of electrolyte-controlled sulfur evolution and offer insight into how mediator chemistry affects sulfur formation, phase behavior, and redistribution in Li–S batteries.

CHAPTER TWO

MATERIALS AND METHODS

2.1 Materials and Chemicals

All chemicals used in this work were analytical grade and used as received without further purification. Lithium bis(trifluoromethanesulfonyl)imide (LiTFSI, 99.95%, Sigma-Aldrich) was employed as the supporting lithium salt, while lithium nitrate ($LiNO_3$, 99.99%, Sigma-Aldrich) was used as a passivating additive to stabilize the lithium metal electrode. Lithium iodide (LiI, anhydrous, 99%, Thermo Scientific) served as the redox mediator for investigating its influence on sulfur evolution. Isopropylxanthic disulfide (DIP) was employed as an organic sulfur-conversion mediator to study its interactions with lithium polysulfides.

Elemental sulfur (S_8, 99.98%, Sigma-Aldrich) and lithium sulfide (Li_2S, 99.9%, Thermo Scientific) were used to prepare lithium polysulfide solutions. The electrolyte solvent consisted of 1,3-dioxolane (DOL) and 1,2-dimethoxyethane (DME) with a volume ratio of 1:1. Lithium foil served as both the counter and reference electrode, while a platinum wire with a diameter of 25 μm was used as the working electrode for sulfur generation. All electrolyte preparation and cell assembly procedures were carried out inside an argon-filled glovebox with oxygen and moisture concentrations below 0.1 ppm to avoid contamination.

2.2 Electrolyte Preparation

2.2.1 Preparation of Lithium Polysulfide Solution

A 5 M lithium polysulfide stock solution was prepared by dissolving elemental sulfur and lithium sulfide in a DOL/DME (1:1 by volume) mixed solvent. The sulfur-to-lithium sulfide ratio corresponded to the stoichiometric composition of Li_2S_8. The mixture was magnetically stirred at 56 °C for approximately 12 h until a homogeneous dark-red solution was obtained. The stock solution was subsequently diluted to the desired concentration before electrochemical experiments.

2.2.2 Preparation of Supporting Electrolyte

The supporting electrolyte consisted of LiTFSI dissolved in DOL/DME (1:1 by volume) together with 2 wt% $LiNO_3$. $LiNO_3$ was added to improve the stability of the lithium metal surface by suppressing undesirable parasitic reactions. The electrolyte was stirred overnight inside the glovebox before use to ensure complete dissolution of all components.

2.2.3 Preparation of LiI Electrolytes

To investigate the influence of LiI concentration on sulfur evolution, LiI was added to the supporting electrolyte at different concentrations. Five electrolyte compositions were prepared:

- 1 M LiTFSI + 2 wt% $LiNO_3$
- 1 M LiTFSI + 0.05 M LiI + 2 wt% $LiNO_3$
- 1 M LiTFSI + 0.10 M LiI + 2 wt% $LiNO_3$
- 1 M LiTFSI + 0.20 M LiI + 2 wt% $LiNO_3$
- 1 M LiI + 2 wt% $LiNO_3$

LiI concentrations of 0.05 M, 0.1 M and 0.20 M were selected to represent the concentration range commonly employed as redox additives in lithium–sulfur batteries. To further investigate the influence of LiI concentration on sulfur evolution beyond the conventional additive range, a 1 M LiI electrolyte was also examined as an iodine-rich condition. This concentration series enabled systematic evaluation of the transition from conventional additive behavior to a LiI-dominated sulfur-conversion environment.

2.2.4 Preparation of DIP-Containing Electrolytes

A DIP-containing electrolyte was prepared by first generating the reduced form of DIP (DIP-Red). DIP and Li_2S were mixed in diglyme at a DIP concentration of 0.2 M with a DIP-to-Li_2S molar ratio of 1:1.2. The mixture was stirred until the reaction was complete, producing a homogeneous dark-colored DIP-Red solution.

The prepared DIP-Red solution was subsequently mixed with the LiTFSI/polysulfide electrolyte to obtain the final electrolyte used in this study. This electrolyte was employed for in situ optical observation, Raman characterization, and visual examination of the reaction mixtures.

2.3 Customized In Situ Optical Electrochemical Cell

A customized in situ optical electrochemical cell was developed to enable simultaneous electrochemical measurements and real-time optical observation of sulfur evolution during battery operation. Unlike conventional coin cells, which prevent direct visualization of electrochemical reactions, the customized cell provides a transparent observation window that allows sulfur nucleation, growth, coalescence, migration, and detachment to be monitored continuously during charging and discharging. The layered

structure of the cell is illustrated in Figure 2.1, while the fabrication procedure is summarized in Figures 2.2–2.4

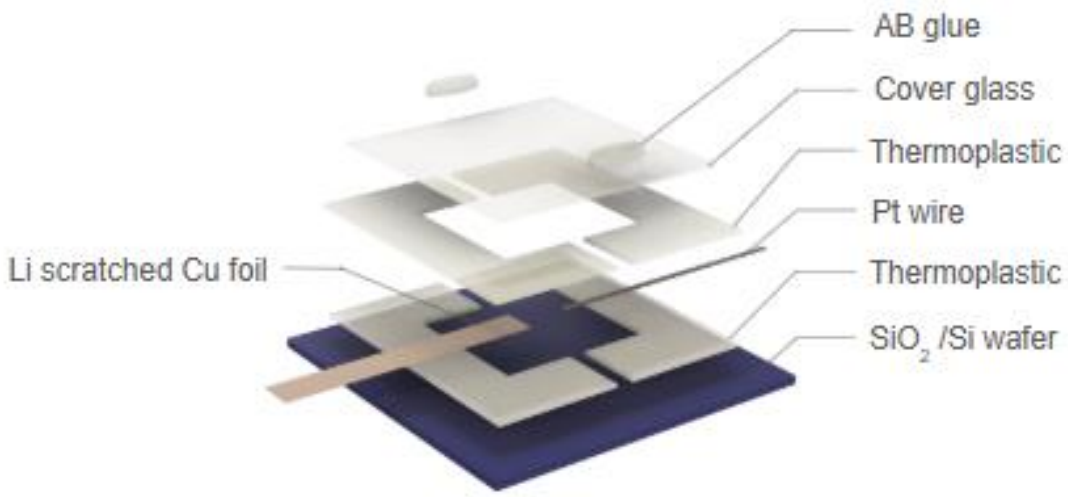

Figure 2.1 Exploded schematic of the customized in situ optical electrochemical cell. The cell was assembled on a SiO_2/Si wafer substrate with an overall size of approximately 2 cm × 3 cm. The active electrolyte chamber was defined by thermoplastic spacers and had an approximate size of 1.2 cm × 1.2 cm × 0.1 cm. The cell contained a platinum wire working electrode, a lithium-coated copper foil counter/reference electrode, a glass coverslip, and epoxy sealing. The transparent optical window enabled real-time observation of sulfur evolution during electrochemical reactions. As shown in Figure 2.1, the customized in situ optical electrochemical cell was assembled on a SiO_2/Si wafer substrate with an overall size of approximately 2 cm × 3 cm. The active electrolyte chamber was defined by thermoplastic spacers and had an approximate size of 1.2 cm × 1.2 cm × 0.1 cm. The cell consisted of a Pt wire working electrode, a lithium-coated copper foil counter/reference electrode, a glass coverslip, and epoxy sealing. The glass

coverslip provided a transparent optical window for real-time microscopic observation of sulfur evolution during electrochemical reactions.

The fabrication process is illustrated in Figure 2.2. The SiO_2/Si wafer was first cut to the desired size using a diamond scribe. Thermoplastic films were then patterned to define the electrolyte chamber. A Pt wire with a diameter of 25 μm was aligned on the substrate and temporarily fixed using the thermoplastic spacer at approximately 90 °C, leaving an exposed length of approximately 6 mm to serve as the working electrode.

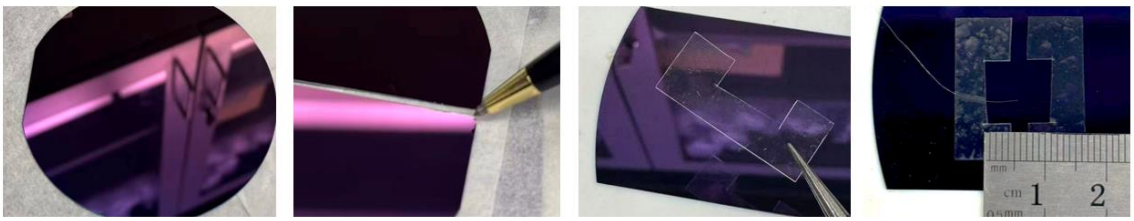

Figure 2.2 Fabrication of the customized in situ optical electrochemical cell. (a) Preparation of the glass wafer. (b) Wafer scribing using a diamond scribe. (c) Patterning of the thermoplastic spacer to define the electrolyte chamber. (d) Preliminary assembly of the optical cell with the Pt wire and patterned thermoplastic spacer.

The lithium counter/reference electrode was prepared separately, as shown in Figure 2.3. Inside an argon-filled glovebox (O_2 and H_2O < 0.1 ppm), a thin lithium foil was mechanically laminated onto a copper current collector to ensure good electrical contact. The laminated lithium was then trimmed to the required dimensions before being positioned opposite the platinum wire.

Figure 2.3 Preparation of the lithium counter electrode. (a) Preparation of the copper current collector. (b) Placement of a lithium foil on the copper current collector. (c) Lamination of the lithium foil onto the copper current collector to ensure good electrical contact. (d) Prepared lithium electrode after trimming to the desired dimensions.

After both electrodes had been assembled, a glass coverslip was placed on top of the cell and bonded by heating the thermoplastic spacer to approximately 110 °C, forming a sealed optical chamber while leaving two openings for electrolyte injection. Approximately 40 µL of electrolyte was subsequently introduced through the openings, allowing the chamber to be filled by capillary action with minimal air entrapment. Finally, the injection ports were sealed using a two-part epoxy adhesive to prevent electrolyte leakage and solvent evaporation during electrochemical measurements. The completed optical electrochemical cell was then ready for in situ optical and electrochemical characterization.

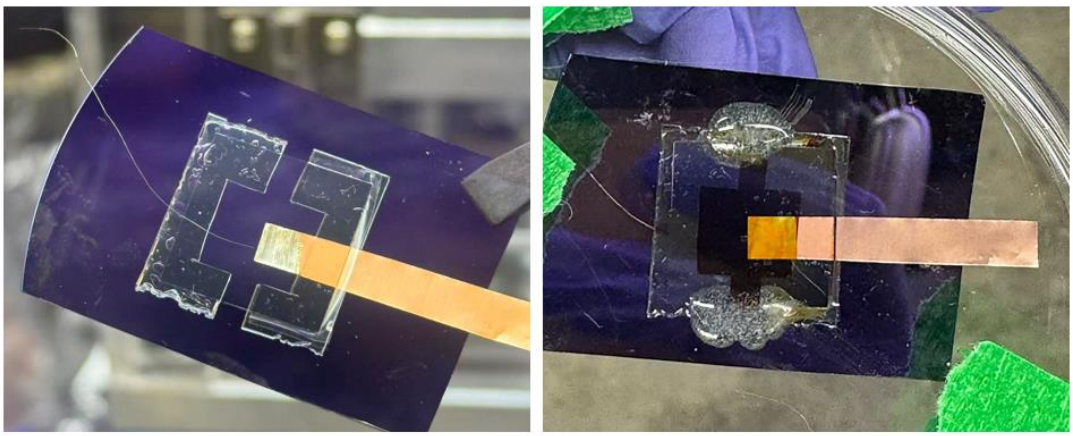

Figure 2.4 Final assembly of the customized in situ optical electrochemical cell. (a) Pre-sealed optical cell after bonding the glass cover, leaving an opening for electrolyte injection. (b) Fully assembled optical electrochemical cell after electrolyte injection and sealing with AB glue.

2.4 Experimental Setup

The experimental setup used for in situ optical electrochemical measurements is illustrated in Figure 2.5. The customized optical electrochemical cell was mounted on the stage of an Olympus BX53M optical microscope. A BioLogic potentiostat was connected to the cell to perform electrochemical measurements, including constant voltage charging, and chronoamperometry.

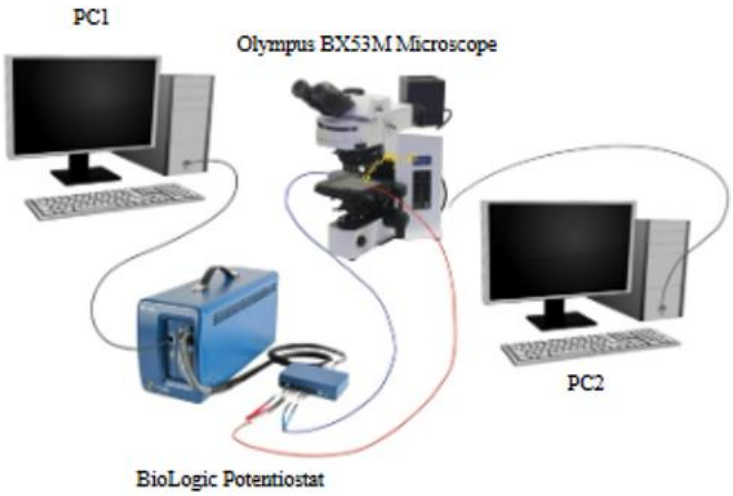

Figure 2.5 Experimental setup for in situ optical electrochemical measurements. The optical cell was mounted on an Olympus BX53M microscope and connected to a BioLogic potentiostat.

During the experiments, the BioLogic potentiostat controlled the electrochemical protocol, while the Olympus BX53M microscope recorded the optical evolution of sulfur using a digital camera. Electrochemical data and optical images were collected simultaneously on two separate computers to avoid interruption during data acquisition. This setup allowed real-time correlation between the electrochemical response and sulfur evolution in the optical cell. As a result, sulfur nucleation, growth, coalescence, migration, and detachment could be directly observed under controlled electrochemical conditions.

2.5 Electrochemical Procedures

Electrochemical experiments were carried out using a BioLogic potentiostat connected to the customized optical cell. Once the cell was assembled and filled with electrolyte, it was immediately connected to the potentiostat and tested. To investigate sulfur evolution

under different electrolyte compositions, a series of constant-voltage charging experiments were performed. For the LiI system, charging voltages ranging from 3.0 to 3.5 V were examined. Sulfur generation was first observed at approximately 3.2 V, while 3.5 V produced the most pronounced sulfur evolution and was therefore selected for most optical observations. After the charging process, a constant-current discharge of −10 μA was applied to reverse sulfur conversion.

For the DIP system, lower charging voltages were also evaluated in an attempt to promote sulfur formation under milder electrochemical conditions. However, distinct sulfur droplet formation was likewise observed only when the charging voltage reached approximately 3.2 V. Consequently, the same charging voltage was adopted for subsequent experiments to enable direct comparison between the LiI and DIP systems.

For the LiI study, sulfur evolution was investigated using electrolytes containing different LiI concentrations. For the DIP study, different DIP-to-Li_2S molar ratios were first investigated to optimize the electrolyte composition for subsequent charging experiments. Because the reaction between DIP and lithium polysulfides depends on the relative concentration of the two reactants, different molar ratios may generate different sulfur-containing intermediates. Based on the preliminary characterization results, a 1:1.2 DIP-to-Li_2S molar ratio was selected for all subsequent electrochemical and in situ optical experiments. Throughout all experiments, optical images and electrochemical data were collected simultaneously to establish the relationship between sulfur evolution behavior and electrochemical conditions.

2.6 In Situ Optical Observation

Real-time optical observation was used to investigate sulfur evolution during electrochemical charging. A digital camera mounted on the optical microscope continuously recorded time-lapse images and videos of the optical electrochemical cell, enabling direct observation of sulfur formation on the Pt wire and within the surrounding electrolyte.

The customized optical platform allowed the temporal and spatial evolution of sulfur droplets to be monitored throughout the charging process. The recorded image sequences captured droplet nucleation, growth, coalescence, and movement. In some cases, droplet displacement and detachment from the Pt wire were also observed. These liquid-like behaviors provide direct visual evidence for the formation of supercooled liquid sulfur during sulfur oxidation. Representative images were selected at defined charging times to compare sulfur evolution under different electrolyte compositions and applied potentials. The comparisons focused on the onset of visible sulfur formation, apparent droplet size, visible droplet density, spatial distribution, and the location of droplets relative to the Pt wire. Particular attention was given to whether droplets remained attached to the electrode or moved into the surrounding electrolyte.

The same nominal microscope magnification was maintained within each comparison, and scale bars were added using the microscope calibration. Because the images were collected at a selected focal plane, droplets located above or below that plane could appear blurred or might not be clearly resolved. Overlapping droplets and droplets located behind the Pt wire could also be difficult to distinguish. Therefore, the optical images were used to identify qualitative trends in sulfur evolution rather than to provide a complete three-dimensional measurement of the droplet population.

For the LiI study, the optical observations were compared with the corresponding current–time responses obtained during potentiostatic charging. This comparison was used to evaluate how LiI concentration influenced the onset, extent, and spatial distribution of visible sulfur generation.

For the DIP-Red study, sulfur evolution was evaluated using in situ optical observation together with Raman spectroscopy and visual examination of the reaction mixtures. The optical analysis focused primarily on sulfur nucleation, droplet growth, displacement, detachment, and redistribution within the electrolyte.

CHAPTER THREE

REGULATION OF SUPERCOOLED LIQUID SULFUR FORMATION BY LiI

3.1 Effect of LiI Concentration on Sulfur Generation

The effect of LiI concentration on supercooled liquid sulfur formation was investigated using the customized in situ optical electrochemical cell. Five electrolyte conditions were examined: 1 M LiTFSI, 1 M LiTFSI with 0.05 M LiI, 1 M LiTFSI with 0.10 M LiI, 1 M LiTFSI with 0.20 M LiI, and an iodine-rich electrolyte containing 1 M LiI. All experiments were conducted under potentiostatic charging at 3.5 V using the same optical cell configuration.

A direct comparison between the baseline 1 M LiTFSI electrolyte and the iodine-rich 1 M LiI electrolyte is shown in Figure 3.1. In the 1 M LiTFSI electrolyte, the sulfur droplets were primarily concentrated on and immediately adjacent to the Pt wire. The droplets formed a dense layer along the electrode, indicating that visible sulfur generation remained localized near the electrode/electrolyte interface.

In contrast, the 1 M LiI electrolyte produced a substantially different spatial distribution. Sulfur droplets were observed both near the Pt wire and over a broader region of the surrounding electrolyte within the selected focal plane. The droplets were less confined to the electrode surface, demonstrating that the presence of a high concentration of iodide extended the sulfur-generation region away from the Pt wire.

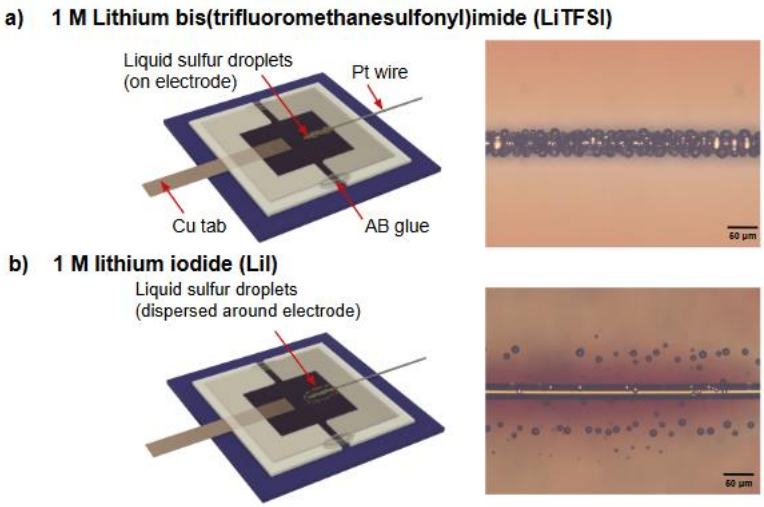

Figure 3.1 Comparison of sulfur-droplet distributions in the baseline and iodine-rich electrolytes during potentiostatic charging at 3.5 V. (a) In the 1 M LiTFSI electrolyte, sulfur droplets were primarily concentrated on and immediately adjacent to the Pt wire. (b) In the 1 M LiI electrolyte, sulfur droplets were distributed over a broader region surrounding the electrode. The optical images show representative droplet distributions within the selected focal plane. Scale bars: 50 µm.

Because the 1 M LiI condition represents an iodine-rich comparison rather than a conventional additive concentration, additional experiments were conducted using lower LiI concentrations of 0.05, 0.10, and 0.20 M. The corresponding time-dependent optical images are presented in Figure 3.2.

At 0.05 M LiI, very few droplets were visible after 10 s of charging. Small droplets began to appear on or immediately adjacent to the Pt wire after approximately 1 min. Their number gradually increased between 1 and 5 min, but the majority of the visible droplets remained concentrated near the electrode. The droplet population was relatively sparse and showed a comparatively narrow spatial distribution.

At 0.10 M LiI, sulfur formation became more pronounced. A denser population of droplets developed along the Pt wire within the first minute, and additional droplets became visible in the surrounding electrolyte at later times. By 3 and 5 min, droplets were present at different distances and focal depths around the wire. The coexistence of sharply focused and blurred droplets indicates that the sulfur population was distributed through more than one depth plane within the optical chamber.

The strongest response within the additive-concentration series was observed at 0.20 M LiI. Numerous droplets were already visible both near and away from the Pt wire after 10 s. The visible droplet density increased rapidly during the first minute and continued to increase at 3 and 5 min. Compared with the 0.05 and 0.10 M LiI electrolytes, the droplets occupied a substantially broader region of the optical field.

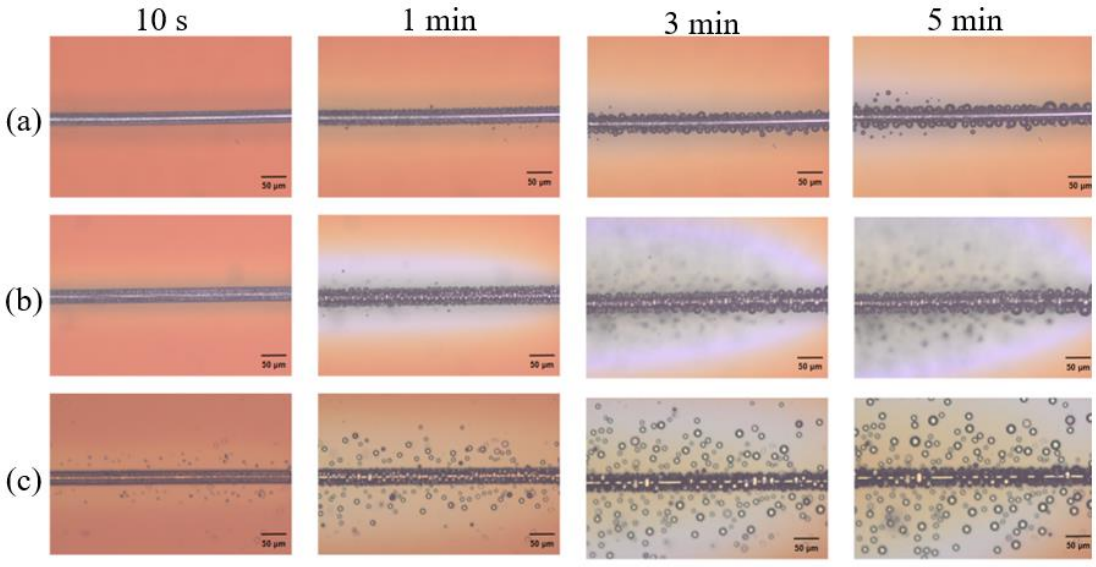

Figure 3.2 Time-dependent optical evolution of sulfur droplets in electrolytes containing different LiI concentrations during potentiostatic charging at 3.5 V. (a) 0.05 M LiI, (b) 0.10 M LiI, and (c) 0.20 M LiI. Images were collected after 10 s, 1 min, 3 min, and 5 min

of charging. Increasing the LiI concentration resulted in earlier visible sulfur formation, a higher visible droplet density, and a broader spatial distribution within the surrounding electrolyte. Scale bars: 50 μm.

The concentration series reveals a clear transition in the location and extent of visible sulfur generation. At 0.05 M LiI, sulfur formation remained largely associated with the Pt wire during the early stage of charging. At 0.10 M LiI, the droplet population became denser and extended farther into the surrounding electrolyte. At 0.20 M LiI, droplets appeared throughout a broad region almost immediately after charging began.

The visible droplet population also became less uniform as the LiI concentration increased. At lower LiI concentration, the images were dominated by relatively small droplets located near the electrode. At higher concentration, droplets of different visible sizes were present both near and away from the Pt wire. This broad size and spatial distribution suggest that sulfur formation occurred at multiple locations and times rather than through uniform growth of a fixed population on the electrode.

A gradual lightening of the electrolyte background was also observed during charging, particularly at higher LiI concentrations. This color change is consistent with the consumption of colored dissolved polysulfide species during oxidation. However, because image intensity was affected by illumination, focal depth, and droplet scattering, the color change was treated only as qualitative supporting evidence and was not used as a quantitative measure of sulfur conversion.

Overall, increasing the LiI concentration shortened the time required for visible sulfur droplets to appear, increased the visible droplet density, and expanded the sulfur-generation region away from the Pt wire. These concentration-dependent observations

support the proposed iodine-mediated pathway discussed in Section 3.4, in which electrochemically generated iodine species enable the oxidation of dissolved polysulfides beyond the immediate electrode surface.

3.2 Morphological Evolution of Supercooled Liquid Sulfur

The in situ optical cell enabled the morphology and motion of sulfur droplets to be followed during potentiostatic charging. Although the spatial location of sulfur generation depended strongly on LiI concentration, the visible droplets exhibited several common liquid-like behaviors, including spherical nucleation, growth, coalescence, movement, and, in some cases, detachment from the Pt wire.

In the baseline and low-LiI electrolytes, the earliest visible droplets generally appeared on or immediately adjacent to the Pt wire. These newly formed droplets exhibited approximately spherical shapes. The spherical morphology is consistent with a liquid phase because interfacial tension tends to minimize the surface area of a liquid droplet in contact with the surrounding electrolyte.

As charging continued, the droplets increased in diameter while maintaining their rounded morphology. At the same time, additional small droplets continued to appear. The simultaneous presence of newly formed small droplets and larger previously formed droplets produced a nonuniform size distribution, indicating that nucleation and growth occurred concurrently.

When neighboring droplets came into contact, they were observed to merge into larger droplets. The merged droplets subsequently returned to an approximately spherical shape. This coalescence and shape relaxation provide strong optical evidence that the observed

sulfur existed as a liquid-like phase during charging rather than as rigid crystalline particles.

Some droplets initially associated with the Pt wire also moved along the electrode surface. In selected experiments, droplets were displaced from the wire and became visible in the surrounding electrolyte. These observations demonstrate that droplets formed at the electrode could undergo migration and detachment after growth.

However, droplets observed away from the Pt wire should not all be interpreted as detached droplets. In the 0.20 M and 1 M LiI electrolytes, off-electrode droplets appeared within the first few seconds of charging and were distributed over a broad region. Their early appearance is more consistent with sulfur generation occurring within the surrounding electrolyte through an iodine-mediated pathway. Therefore, two processes may contribute to droplets located away from the electrode: direct sulfur formation within the electrolyte and detachment of droplets that initially formed on the Pt wire.

The relative importance of these processes changed with LiI concentration. At low LiI concentration, sulfur generation remained predominantly localized near the electrode, and the observed evolution was dominated by nucleation and growth along the Pt wire. At higher LiI concentration, the rapid appearance of droplets throughout the surrounding electrolyte became increasingly important, producing a higher visible droplet density and a broader spatial distribution.

The observed spherical morphology, coalescence, shape relaxation, and droplet mobility are consistent with the formation of supercooled liquid sulfur. Raman characterization presented later in this work provides complementary chemical evidence that the optically observed droplets were elemental sulfur. Together, the optical and spectroscopic results

support the identification of the droplets as supercooled liquid sulfur rather than conventional crystalline sulfur precipitates.

Overall, sulfur evolution involved a combination of nucleation, growth, coalescence, migration, and detachment. However, the location and relative contribution of these processes depended on the LiI concentration. The corresponding electrochemical responses are examined in the following section.

3.3 Electrochemical Response during Potentiostatic Charging

In addition to the optical observations, the current response was recorded during potentiostatic charging at 3.5 V to compare the electrochemical behavior of electrolytes containing different LiI concentrations. The resulting current–time profiles are shown in Figure 3.3.

The baseline 1 M LiTFSI electrolyte exhibited the lowest current throughout the charging period. After LiI was introduced, the measured anodic current increased, and a general concentration-dependent trend was observed among the mixed-salt electrolytes. The electrolyte containing 0.20 M LiI produced the highest current among the 0.05, 0.10, and 0.20 M LiI conditions, followed by the 0.10 and 0.05 M LiI electrolytes.

The iodine-rich 1 M LiI electrolyte exhibited a substantially larger and more sustained current response than the other electrolyte compositions. Its current remained above approximately 0.14 mA near the end of the measurement, whereas the mixed-salt electrolytes gradually decreased to considerably lower values. A change in slope was also observed near 200 s for the 1 M LiI electrolyte, indicating a change in the dominant electrochemical or mass-transport behavior during charging.

The higher and more sustained anodic current observed with increasing LiI concentration is consistent with the optical results. Electrolytes containing more LiI showed earlier visible sulfur formation, a greater droplet population, and a broader sulfur-generation region. These results indicate that LiI increased the extent of oxidation occurring during potentiostatic charging.

However, the measured current represents the combined contribution of all electrochemical processes occurring in the cell, including iodide oxidation and polysulfide conversion. Therefore, the current response should not be interpreted as a direct quantitative measurement of elemental sulfur production. Instead, it provides supporting electrochemical evidence for the concentration-dependent sulfur-evolution behavior observed by optical microscopy.

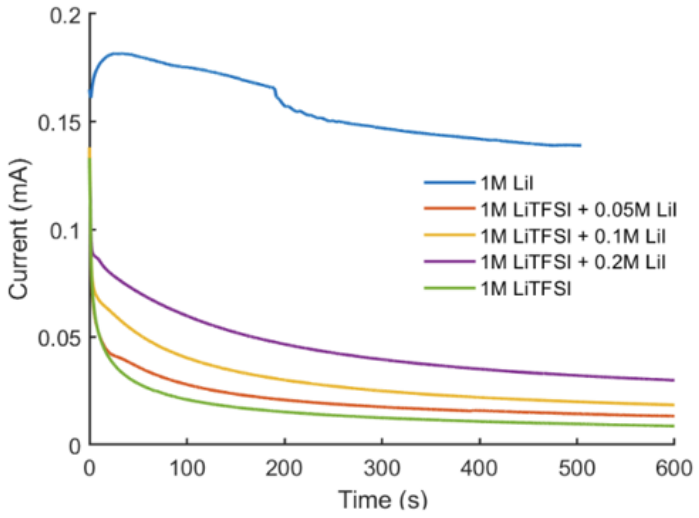

Figure 3.3 Current–time responses of electrolytes containing different LiI concentrations during potentiostatic charging at 3.5 V.

The anodic current generally increased with LiI concentration. The iodine-rich 1 M LiI electrolyte exhibited the largest and most sustained current response, whereas the baseline 1 M LiTFSI electrolyte showed the lowest current.

The combined optical and electrochemical results demonstrate that increasing the LiI concentration changes both the spatial distribution of sulfur formation and the overall anodic response of the cell. These observations provide the experimental basis for the iodine-mediated sulfur-generation mechanism proposed in the following section.

3.4 Proposed Mechanism of LiI-Regulated Supercooled Liquid Sulfur Formation

The optical observations presented in the previous sections demonstrate that LiI fundamentally alters sulfur evolution during electrochemical charging. Compared with the LiTFSI electrolyte, sulfur generation in the presence of LiI extends well beyond the vicinity of the Pt wire, producing a larger number of sulfur droplets distributed throughout the electrolyte. Based on these experimental observations together with previous studies, a mechanism describing LiI-regulated supercooled liquid sulfur formation is proposed.

In the LiTFSI electrolyte, sulfur is primarily generated through the direct electrochemical oxidation of dissolved lithium polysulfides at the Pt wire. Consequently, sulfur nucleation occurs mainly at the electrode/electrolyte interface, and the resulting sulfur droplets remain concentrated near the working electrode throughout most of the charging process.

After LiI is introduced into the electrolyte, iodide ions (I^-)are first electrochemically oxidized at the Pt wire according to

$$2\,I^- \rightarrow I_2 + 2e^-$$

The generated iodine subsequently diffuses into the surrounding electrolyte, where it chemically oxidizes dissolved lithium polysulfides to elemental sulfur while being reduced back to iodide. The regenerated I^- can then participate in subsequent electrochemical oxidation at the electrode surface. In this way, LiI acts as a redox mediator during sulfur conversion.

Unlike direct electrochemical oxidation, which is confined to the electrode/electrolyte interface, the iodine-mediated pathway allows sulfur generation to extend into the surrounding electrolyte wherever dissolved polysulfides are present. The proposed pathway is illustrated in Figure 3.4.

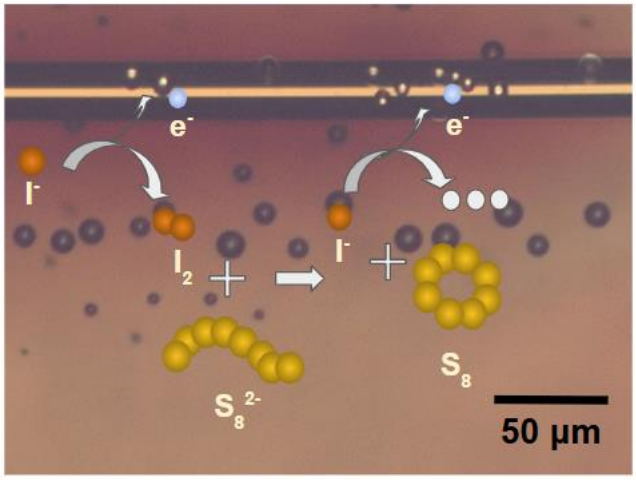

Figure 3.4 Proposed iodine-mediated pathway for sulfur generation in the LiI-containing electrolyte. Iodide is electrochemically oxidized to iodine at the Pt wire. The generated iodine diffuses into the surrounding electrolyte and chemically oxidizes dissolved polysulfides to elemental sulfur while being reduced back to iodide. This redox-mediation pathway extends sulfur generation beyond the immediate electrode surface. The optical observations support this interpretation. Compared with the LiTFSI electrolyte, sulfur droplets appeared over a broader region after LiI was introduced, and

the visible sulfur-generation region expanded as the LiI concentration increased. At higher LiI concentrations, droplets appeared earlier, the visible droplet density increased, and sulfur formation became less confined to the Pt wire.

The concentration-dependent sulfur evolution can be qualitatively interpreted using classical nucleation theory. Although sulfur nucleation in the present system most likely occurs heterogeneously at the electrode/electrolyte interface, classical nucleation theory provides a useful framework for understanding how sulfur supersaturation influences sulfur nucleation and the subsequent formation of supercooled liquid sulfur droplets. According to classical nucleation theory, the formation of a stable sulfur nucleus requires overcoming a thermodynamic free-energy barrier,

$$\Delta G^* = \frac{16\pi\gamma^3}{3(\Delta G_v)^2} \tag{3-1}$$

where γ is the sulfur/electrolyte interfacial energy and $\Delta G_v is$the volumetric free-energy change associated with sulfur formation. The thermodynamic driving force is related to sulfur supersaturation by

$$\Delta G_v = -\frac{RT \ln S}{V_m} \tag{3-2}$$

where S is the sulfur supersaturation ratio, R is the universal gas constant, T is the absolute temperature, and $V_m$is the molar volume of sulfur. An increase in sulfur supersaturation increases the thermodynamic driving force for sulfur nucleation, thereby reducing the nucleation barrier.

The corresponding critical nucleus radius is given by

$$r^* = \frac{2\gamma}{|\Delta G_v|} \tag{3-3}$$

indicating that a higher sulfur supersaturation decreases the critical nucleus size required for stable sulfur formation. The nucleation rate can therefore be expressed as

$$J = J_0 \exp\left(-\frac{\Delta G^*}{kT}\right) \quad (3\text{-}4)$$

where J is the nucleation rate, $J_0$is the kinetic prefactor, and k is the Boltzmann constant. Because the nucleation rate depends exponentially on the nucleation barrier, even a modest reduction in $\Delta G^{\backslash astresults}$in a substantial increase in sulfur droplet nucleation. According to classical nucleation theory, sulfur nucleation is primarily governed by three thermodynamic factors: the sulfur/electrolyte interfacial energy (γ), the thermodynamic driving force represented by sulfur supersaturation (ΔG_v), and temperature (T). In the present study, all experiments were performed using the same electrolyte solvent and at the same operating temperature. Therefore, the sulfur/electrolyte interfacial energy and temperature are assumed to remain approximately constant. Under these conditions, the observed differences in sulfur nucleation are mainly attributed to changes in sulfur supersaturation introduced by the iodine-mediated sulfur-conversion pathway.

In the LiI-containing electrolyte, the continuous chemical oxidation of dissolved lithium polysulfides by iodine generates sulfur throughout the electrolyte rather than only at the electrode surface. Consequently, the local sulfur concentration increases, producing a higher sulfur supersaturation than that in the LiTFSI electrolyte. According to classical nucleation theory, the increased sulfur supersaturation decreases both the nucleation barrier and the critical nucleus radius while simultaneously increasing the nucleation rate. This theoretical interpretation agrees well with the real-time optical visualization and

electrochemical measurements showing increased sulfur droplet number, larger sulfur coverage, and broader sulfur distribution with increasing LiI concentration.

Following nucleation, sulfur evolution proceeds through a continuous sequence of droplet growth, coalescence, migration, and detachment. Newly generated sulfur continuously supplies existing droplets, allowing them to grow throughout charging. Neighboring droplets subsequently merge into larger droplets, while some droplets migrate along the Pt wire before detaching into the surrounding electrolyte. These dynamic behaviors are characteristic of a liquid phase and provide direct evidence that sulfur initially exists as supercooled liquid droplets before eventually transforming into solid sulfur.

Overall, the experimental observations indicate that LiI regulates sulfur evolution through an iodine-mediated sulfur-conversion pathway. Rather than simply accelerating sulfur oxidation, LiI increases sulfur supersaturation throughout the electrolyte, thereby promoting sulfur nucleation and facilitating the formation of supercooled liquid sulfur. These findings provide direct experimental evidence that electrolyte additives can regulate sulfur nucleation by modifying local sulfur supersaturation, offering a new perspective for understanding and controlling supercooled liquid sulfur formation in lithium–sulfur batteries.

3.5 Summary

In this chapter, the effect of LiI on the formation and evolution of supercooled liquid sulfur was systematically investigated using a customized in situ optical electrochemical cell. By combining real-time optical visualization and Raman characterization, the role of LiI in sulfur evolution was evaluated from both qualitative and quantitative perspectives.

A comparison between LiTFSI and LiI electrolytes showed that sulfur generation in the LiTFSI electrolyte remained primarily confined to the Pt wire, whereas sulfur formation in the LiI electrolyte extended throughout the surrounding electrolyte. This difference indicates that LiI fundamentally changes the sulfur-generation behavior during electrochemical charging.

The influence of LiI concentration was further examined using time-resolved optical observations. Increasing the LiI concentration accelerated sulfur evolution, expanded the sulfur-generation region, and promoted the formation of larger sulfur droplets with broader spatial distribution.

Based on the experimental observations and previous studies, a LiI-regulated sulfur-conversion mechanism was proposed. Electrochemically generated iodine species diffuse into the electrolyte and chemically oxidize dissolved lithium polysulfides, allowing sulfur to be generated throughout the electrolyte rather than only at the electrode surface. The increased sulfur concentration promotes the nucleation and evolution of supercooled liquid sulfur droplets, resulting in the dynamic processes of droplet growth, coalescence, migration, and detachment observed during charging.

Overall, this chapter demonstrates that LiI influences not only the amount of sulfur generated but also the location and evolution behavior of sulfur during charging. The mechanistic understanding obtained in this chapter provides the foundation for the following chapter, where an alternative sulfur-conversion strategy based on DIP is investigated.

CHAPTER FOUR

EFFECT OF DIP ON SULFUR CONVERSION

4.1 Optimization of DIP-Red Solution Preparation

Before investigating the influence of DIP-Red on sulfur evolution, the preparation conditions were optimized to obtain a reproducible solution while minimizing the formation of insoluble reaction products. The effects of the sulfur source, solvent system, DIP concentration, and DIP-to-reducing-agent molar ratio were evaluated.

Initial experiments were performed by directly reacting DIP with dissolved lithium polysulfides, Li_2S_8. The reaction occurred rapidly after mixing and produced a visible yellow precipitate at the bottom of the vial. The formation of this precipitate was undesirable for subsequent optical experiments because suspended or deposited particles could interfere with the observation and identification of electrochemically generated sulfur droplets.

The rapid reaction between DIP and dissolved Li_2S_8 may result in the local accumulation of sulfur-rich products, including elemental sulfur, before these products can remain dissolved as polysulfide species. This process may account for the formation of the visible yellow precipitate. However, the exact chemical composition of the precipitate was not independently determined in this work. Therefore, it is referred to here as a yellow reaction-derived precipitate rather than being assigned to a specific sulfur species.

To reduce the formation of this precipitate, Li_2S was used instead of Li_2S_8 for subsequent DIP-Red preparation. Compared with dissolved Li_2S_8, Li_2S has limited solubility in

diglyme, and the reaction proceeded more gradually. No comparable yellow reaction-derived precipitate was observed under the selected Li_2S-based preparation conditions. Any elemental sulfur formed during the reaction between DIP and Li_2S may further react with Li_2S to produce dissolved lithium polysulfides, Li_2S_x, according to the general reaction

$$L\,\mathrm{i}_2\,S + (x-1)S \rightarrow L\,\mathrm{i}_2\,\mathrm{S}_x$$

The formation of dissolved polysulfide species is consistent with the yellow-brown to reddish-brown appearance of the resulting solutions. This secondary reaction may reduce the accumulation of elemental sulfur as a separate solid phase and therefore limit the formation of the visible yellow precipitate observed in the DIP–Li_2S_8 system. However, the specific polysulfide chain lengths and solution compositions were not directly identified in this work.

A series of DIP-Red solutions was prepared in diglyme using 0.2 M DIP with DIP-to-Li_2S molar ratios of 1:0.8, 1:1, 1:1.2, and 1:1.5. A visual comparison of the resulting solutions is shown in Figure 4.1. The solutions prepared at ratios of 1:0.8 and 1:1 exhibited a darker reddish-brown color. In comparison, the 1:1.2 and 1:1.5 solutions showed a similar yellow-brown appearance.

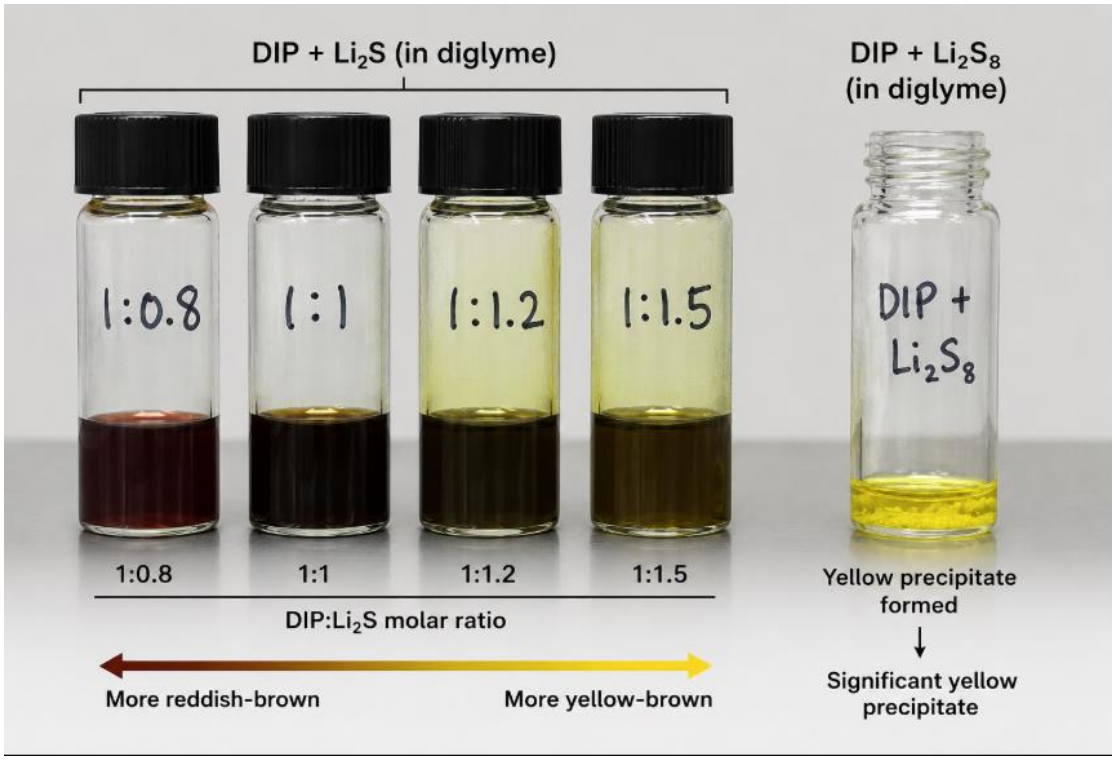

Figure 4.1 Visual comparison of DIP-Red preparation using Li_2S and Li_2S_8. The four capped vials contain 0.2 M DIP solutions prepared with DIP-to-Li_2S molar ratios of 1:0.8, 1:1, 1:1.2, and 1:1.5, from left to right. The 1:0.8 and 1:1 samples exhibited a darker reddish-brown color, whereas the Li_2S-excess samples exhibited a similar yellow-brown appearance. The uncapped vial on the right shows the reaction mixture prepared using DIP and Li_2S_8, in which a visible yellow precipitate formed.

The color difference suggests that the relative amount of Li_2S influenced the composition of the dissolved sulfur-containing species. The similar appearance of the 1:1.2 and 1:1.5 samples indicate that increasing the Li_2S content beyond a slight excess did not produce an obvious additional visual change. Nevertheless, solution color was used only as a

qualitative indicator and was not considered direct evidence of a specific Li_2S_x composition or complete DIP reduction.

A DIP-to-Li_2S molar ratio of 1:1.2 was selected for subsequent experiments. This formulation provided a slight excess of Li_2S, which reduced the likelihood of leaving a substantial amount of unreacted DIP in the solution. The excess Li_2S also allowed any sulfur formed during the reaction to further react and remain in solution as lithium polysulfide species. Compared with the 1:1.5 formulation, the 1:1.2 ratio provided the desired Li_2S excess without introducing an unnecessarily large amount of residual solid. Because Li_2S was added in excess and is only partially soluble in diglyme, some solid material remained at the bottom of the vial after the reaction. This sediment was visually different from the yellow reaction-derived precipitate observed in the DIP–Li_2S_8 system and was attributed primarily to excess, poorly dissolved Li_2S. The reaction mixture was therefore allowed to settle, and only the upper supernatant was collected for subsequent electrolyte preparation.

The optimized DIP-Red preparation consisted of 0.2 M DIP and Li_2S at a DIP-to-Li_2S molar ratio of 1:1.2 in diglyme. The collected supernatant was mixed with the polysulfide/LiTFSI electrolyte and used consistently in the subsequent optical, electrochemical, and spectroscopic experiments. This procedure minimized the introduction of suspended solid particles into the optical cell and improved the reproducibility of the DIP-Red-containing electrolyte.

4.2 Optical Observation of Sulfur Evolution in the Presence of DIP-Red

The influence of DIP-Red on sulfur evolution was investigated using the customized in situ optical electrochemical cell. The supernatant collected from the optimized DIP-Red

preparation was mixed with the polysulfide/LiTFSI electrolyte, and sulfur formation was recorded during potentiostatic charging. Control electrolytes containing the same solvent composition but without DIP-Red were tested under comparable conditions to separate the influence of DIP-Red from that of the added glyme solvent.

4.2.1 Triglyme based electrolyte at 3.0 V

Figure 4.2 compares sulfur evolution in the triglyme-containing control electrolyte and the corresponding DIP-Red-containing electrolyte during potentiostatic charging at 3.0 V. In the control electrolyte, no clearly resolved droplets were observed after 10 s, and only a small number of droplets appeared near the Pt wire after 1 min. More distinct droplets became visible after 3 min, but the droplet population remained relatively sparse and was concentrated near the electrode surface throughout the 5 min observation period.

In contrast, small droplets were already visible along the Pt wire in the DIP-Red-containing electrolyte after 10 s. By 1 min, the visible droplet density had increased substantially, and several droplets were located away from the immediate surface of the Pt wire. Within the time resolution of the image sequence, this indicates that droplet displacement or detachment occurred no later than approximately 1 min. Continued charging produced both an increase in the number of visible droplets and the growth of existing droplets.

At 3 and 5 min, the DIP-Red-containing electrolyte exhibited a broad droplet-size distribution. Numerous small droplets remained near the Pt wire, while larger droplets were observed both on and away from the electrode. Based on comparison with the 50 μm scale bar, the early droplets were generally only a few micrometers in diameter, whereas several later-stage droplets reached dimensions on the order of tens of

micrometers. The coexistence of small and large droplets indicates that the droplet population was not uniform and is consistent with continued nucleation occurring simultaneously with droplet growth and possible coalescence.

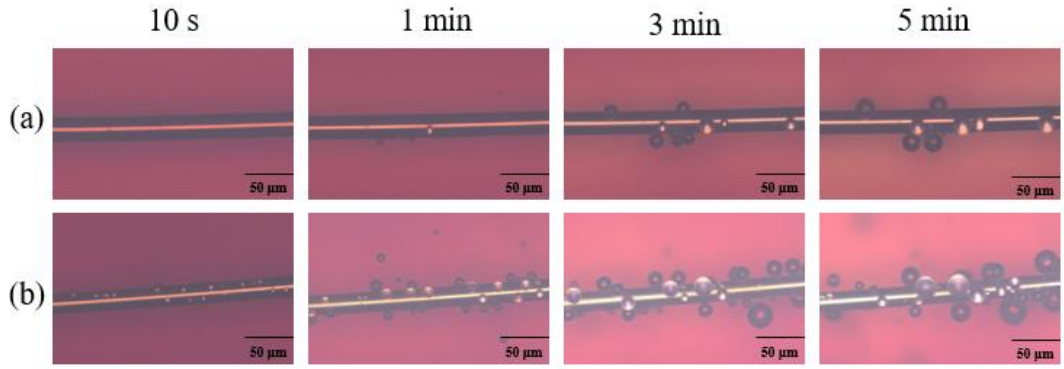

Figure 4.2 Time-dependent optical evolution of sulfur droplets during potentiostatic charging at 3.0 V. (a) Triglyme-containing PS/LiTFSI control electrolyte without DIP-Red. (b) Corresponding DIP-Red-containing PS/LiTFSI electrolyte. Images were collected after 10 s, 1 min, 3 min, and 5 min of charging. The DIP-Red-containing electrolyte exhibited earlier visible droplet formation, a higher visible droplet density, and more pronounced droplet growth. Scale bars: 50 µm.

These observations show that, at 3.0 V, DIP-Red produced a measurable change in both the onset and subsequent evolution of visible sulfur droplets. The primary difference was not a change in the initial nucleation location, because droplets still first appeared near the Pt wire. Instead, DIP-Red increased the extent of droplet growth and promoted the appearance of droplets away from the electrode surface.

4.2.2 Triglyme-based electrolyte at 3.5 V

The influence of the applied potential was further examined by increasing the charging voltage to 3.5 V. As shown in Figure 4.3, sulfur-droplet formation became more

pronounced in both the control and DIP-Red-containing electrolytes. In the control electrolyte, a dense layer of small droplets was already visible along the Pt wire after 10 s. These droplets gradually increased in size during charging, and larger droplets became apparent after 3 and 5 min.

The DIP-Red-containing electrolyte showed a more rapid transition from small droplets to a highly nonuniform droplet population. Numerous droplets were visible along the Pt wire at 10 s, while substantially larger droplets appeared within the first minute. By 3 and 5 min, the image contained both large droplets attached to the wire and smaller droplets distributed around the electrode. The visible size distribution was broader than that observed in the control electrolyte, with droplets ranging from a few micrometers to several tens of micrometers.

The higher charging potential therefore increased the extent of sulfur generation in both electrolytes. The stronger droplet response at 3.5 V cannot be attributed solely to DIP-Red because the control electrolyte also exhibited substantially greater droplet formation than at 3.0 V. Nevertheless, comparison at the same potential shows that the DIP-Red-containing electrolyte developed a larger population of large droplets and a more heterogeneous size distribution over the same charging period.

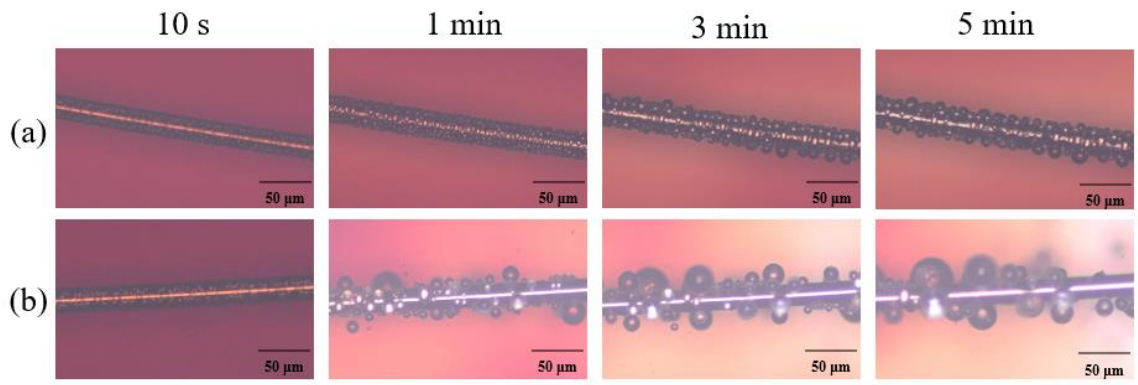

Figure 4.3 Time-dependent optical evolution of sulfur droplets during potentiostatic charging at 3.5 V. (a) Triglyme-containing PS/LiTFSI control electrolyte without DIP-Red. (b) Corresponding DIP-Red-containing PS/LiTFSI electrolyte. Images were collected after 10 s, 1 min, 3 min, and 5 min of charging. Both electrolytes exhibited sulfur-droplet formation, while the DIP-Red-containing electrolyte showed more pronounced droplet growth and a broader visible droplet-size distribution. Scale bars: 50 µm.

Comparison of Figures 4.2 and 4.3 demonstrates that the applied potential strongly influenced the visible droplet density and growth rate. Increasing the potential from 3.0 to 3.5 V shortened the time required for a dense droplet population to develop and produced larger droplets in both electrolytes. The effect of DIP-Red was therefore evaluated through comparisons performed at the same applied potential rather than by directly comparing images collected at different voltages.

4.2.3 Diglyme-based electrolyte

A separate set of experiments was conducted using diglyme-based electrolytes to determine whether the DIP-Red effect was maintained in a different solvent environment.

Figure 4.4 compares a diglyme-containing control electrolyte at 3.2 V, a DIP-Red-containing electrolyte at 3.2 V, and a DIP-Red-containing electrolyte at 3.5 V.

At 3.2 V, the diglyme control electrolyte showed gradual droplet development along the Pt wire. The droplets remained closely associated with the electrode and exhibited a comparatively narrow size distribution during the early stages of charging. Even after 10 min, most visible droplets remained concentrated around the wire, although their size had increased.

Under the same applied potential, the DIP-Red-containing electrolyte exhibited a different progression. Small droplets were visible near the wire after 10 s, followed by an increase in both droplet density and size between 1 and 3 min. By 10 min, several large droplets were visible away from the immediate Pt-wire surface. The appearance of these separated droplets indicates that displacement and detachment occurred during continued charging. The droplet population also became increasingly polydisperse, with large droplets coexisting with numerous smaller droplets.

Increasing the potential of the DIP-Red-containing electrolyte to 3.5 V produced the strongest droplet response. A dense population of droplets developed within the first minute, and large droplets were already present by 3 min. At 10 min, numerous droplets were distributed throughout the visible field rather than being confined to the Pt wire. The image contained both large droplets several tens of micrometers in diameter and a substantial number of smaller droplets. This broad size distribution is consistent with continued formation of new droplets while previously formed droplets continued to grow, detach, and move away from the electrode.

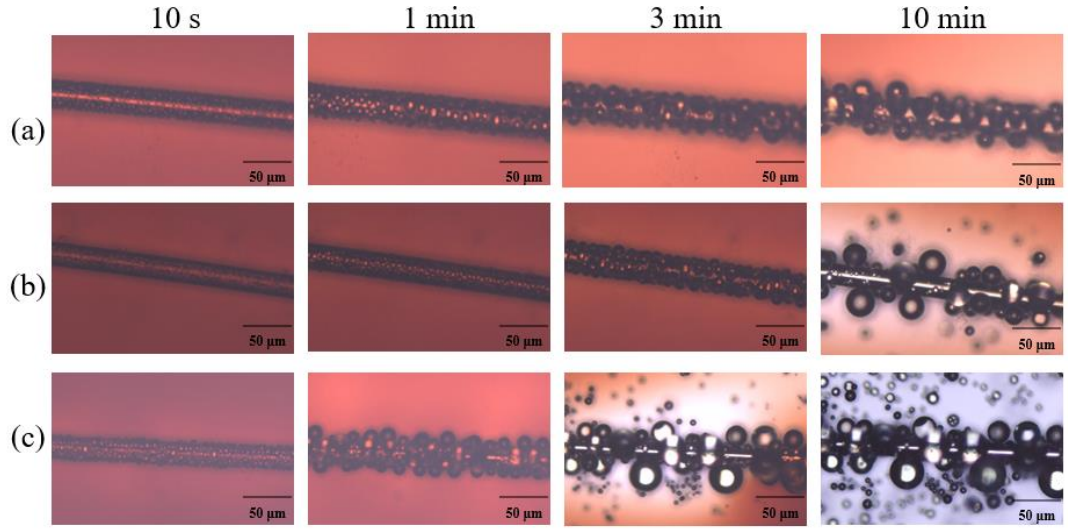

Figure 4.4 Time-dependent optical evolution of sulfur droplets in diglyme-based electrolytes under different charging conditions. (a) PS/LiTFSI electrolyte containing diglyme without DIP-Red, tested at 3.2 V. (b) DIP-Red-containing PS/LiTFSI electrolyte tested at 3.2 V. (c) DIP-Red-containing PS/LiTFSI electrolyte tested at 3.5 V. Images were collected after 10 s, 1 min, 3 min, and 10 min of potentiostatic charging. At 3.2 V, DIP-Red increased the visible droplet growth and promoted the appearance of droplets away from the Pt wire. Increasing the potential to 3.5 V further increased the visible droplet density and broadened the droplet-size distribution. Scale bars: 50 µm.

4.2.4 Overall optical behavior

Across both triglyme- and diglyme-based systems, sulfur droplets initially formed on or near the Pt wire, indicating that the initial sulfur-generation process remained associated with electrochemical oxidation at the electrode/electrolyte interface. However, the subsequent droplet behavior was clearly affected by the presence of DIP-Red.

In the control electrolytes, most droplets remained closely associated with the Pt wire during the observation period. In contrast, the DIP-Red-containing electrolytes showed

repeated displacement and detachment of droplets from the electrode surface. Detached droplets were observed in the surrounding electrolyte and, at later stages, at different depths within the optical chamber. This behavior was most evident at longer charging times and higher applied potentials, when large droplets coexisted with numerous smaller droplets away from the Pt wire.

The presence of both small newly formed droplets and larger detached droplets indicates that sulfur evolution occurred continuously through nucleation, growth, displacement, and detachment. The nonuniform droplet-size distribution further suggests that new droplet formation and the growth of previously formed droplets occurred simultaneously rather than through uniform growth of a fixed droplet population.

The observed detachment behavior provides direct optical evidence that DIP-Red effectively modifies sulfur-droplet evolution after nucleation. Although DIP-Red did not change the initial nucleation location, it promoted the release and redistribution of sulfur droplets from the Pt wire into the surrounding electrolyte. Therefore, the primary effect of DIP-Red in the present system was not the initiation of sulfur formation throughout the bulk electrolyte, but the regulation of droplet growth, detachment, and transport after sulfur had formed at the electrode surface.

This distinction is important because persistent accumulation of sulfur droplets on the Pt wire may increasingly cover the electrode surface during charging. By promoting droplet detachment, DIP-Red may reduce prolonged droplet retention at the electrode and allow continued sulfur formation at newly exposed regions of the Pt surface. Further quantitative measurements of surface coverage and detachment frequency are required to confirm this effect.

Overall, the optical results demonstrate that DIP-Red was effective in promoting sulfur-droplet detachment and redistribution. This behavior distinguishes DIP-Red from the solvent controls and from the LiI-mediated system, and confirms that DIP-Red regulates supercooled liquid sulfur primarily through post-nucleation droplet evolution.

4.3 Raman Identification of Sulfur Products

Raman spectroscopy was used to identify the sulfur species generated during the DIP-Red experiments. Two types of samples were examined: droplets produced in the optical electrochemical cell and the solid product collected after reacting DIP with Li_2S. Commercial sulfur powder was used as a reference.

Raman spectroscopy was first performed on the droplets generated during charging in the optical electrochemical cell. The resulting spectrum was compared with that of commercial sulfur powder, as shown in Figure 4.5. The optically generated droplets exhibited characteristic Raman bands near 150, 220, and 470 cm-1, which were also present in the sulfur reference.

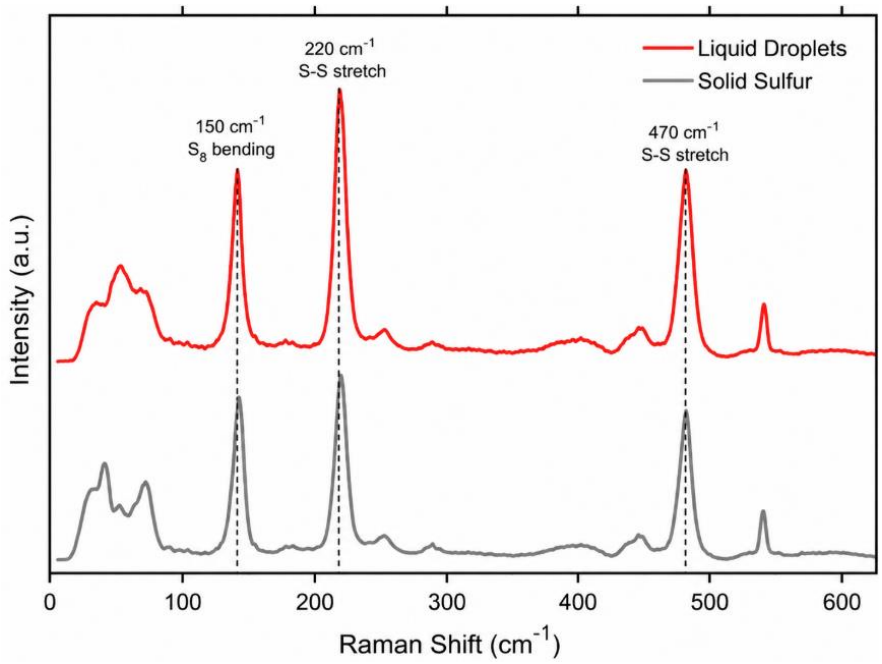

Figure 4.5 Raman spectra of the droplets generated in the optical electrochemical cell and commercial sulfur powder. The characteristic bands near 150, 220, and 470 cm^{-1} are assigned to vibrational modes of elemental sulfur.

The agreement in Raman peak positions confirms that the droplets observed in the optical cell contained elemental sulfur. When combined with their spherical morphology, droplet growth, detachment, and movement in the electrolyte, the Raman results support their identification as supercooled liquid sulfur droplets.

Raman spectroscopy was also performed on the solid product collected after reacting DIP with Li_2S during the preparation of the DIP-Red solution. The spectrum of the reaction product was compared with that of commercial sulfur powder, as shown in Figure 4.6.

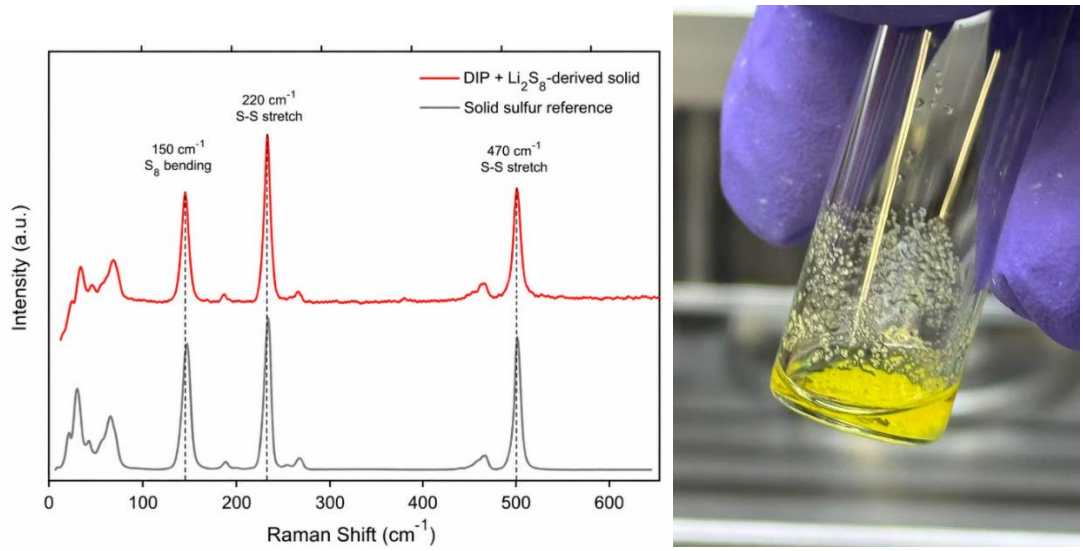

Figure 4.6 Raman spectra of the solid product collected after reacting DIP with Li_2S and commercial sulfur powder. The reaction product exhibited sulfur-related Raman bands near 150, 220, and 470 cm-1, although the peak intensities were lower than those of the sulfur reference.

The solid reaction product exhibited Raman bands at positions similar to those of elemental sulfur, indicating that sulfur-containing products were formed during the reaction between DIP and Li_2S. The Raman signals of the reaction product were weaker than those of commercial sulfur powder. However, Raman intensity is affected by sample quantity, laser focus, surface morphology, collection geometry, and background signal. Therefore, the difference in peak intensity was not used as a quantitative measure of sulfur content. Instead, the agreement in peak positions was used to identify elemental sulfur in the reaction product.

These results provide chemical evidence for two observations in the DIP-Red system. First, the droplets formed in the optical electrochemical cell were identified as elemental sulfur. Second, elemental sulfur was also present in the solid product formed during the

preparation of DIP-Red. The Raman measurements therefore support the interpretation of sulfur evolution during both the chemical preparation and electrochemical testing processes.

4.4 Proposed Role of DIP-Red in Sulfur Evolution

The results presented in this chapter indicate that DIP-Red influences sulfur evolution differently from LiI. This interpretation is based on the combined optical observations, Raman characterization, and visual examination of the reaction mixtures. Because the molecular reactions involving DIP-Red were not directly identified in this work, the discussion in this section focuses on its experimentally observed influence on sulfur formation and droplet evolution.

DIP-Red was prepared by reacting DIP with Li_2S in diglyme. After the reaction mixture was allowed to settle, the supernatant was collected and introduced into the LiTFSI/polysulfide electrolyte. During potentiostatic charging, the earliest visible sulfur droplets appeared on or immediately adjacent to the Pt wire. This observation indicates that initial sulfur generation remained closely associated with electrochemical oxidation at the electrode/electrolyte interface.

This behavior differed from that observed in the LiI-containing electrolyte. In the LiI system, sulfur droplets appeared over a broader region of the electrolyte, consistent with iodine-mediated oxidation of dissolved polysulfides away from the Pt wire. In contrast, immediate sulfur formation throughout the surrounding electrolyte was not observed in the DIP-Red-containing system. DIP-Red therefore did not produce the same spatially distributed sulfur-generation behavior as LiI.

After nucleation on the Pt wire, the sulfur droplets continued to grow during charging. Previously formed droplets were gradually displaced as additional sulfur accumulated near the electrode surface. Some droplets subsequently detached from the Pt wire and moved into the surrounding electrolyte while maintaining an approximately spherical morphology. Detached droplets were also observed at different depths within the optical chamber. These observations establish a sequence of nucleation, growth, displacement, detachment, and transport in the DIP-Red-containing electrolyte.

The repeated observation of droplet detachment represents the clearest optical evidence of the influence of DIP-Red. In the corresponding solvent controls, sulfur droplets generally remained more closely associated with the Pt wire during the same observation period. In the presence of DIP-Red, larger droplets and detached droplets appeared more readily in the surrounding electrolyte. DIP-Red therefore appears to affect the post-nucleation evolution and redistribution of sulfur rather than changing the initial location of sulfur formation.

Raman spectroscopy confirmed that the droplets generated in the optical cell exhibited characteristic features of elemental sulfur. However, Raman measurements did not directly identify the interaction between DIP-Red and dissolved polysulfides. The present results therefore do not establish whether DIP-Red acts through direct electron transfer, coordination with sulfur species, or another intermediate reaction pathway.

Previous work proposed that DIP undergoes reductive activation to form DIP-Red and DIP-Red (Meso) species. These reduced species were proposed to interact with solid lithium polysulfides and mediate electron transfer during sulfur conversion. The

literature-proposed evolution of DIP-derived mediator species is shown in Figure 4.7 (Zhang et al., 2026).

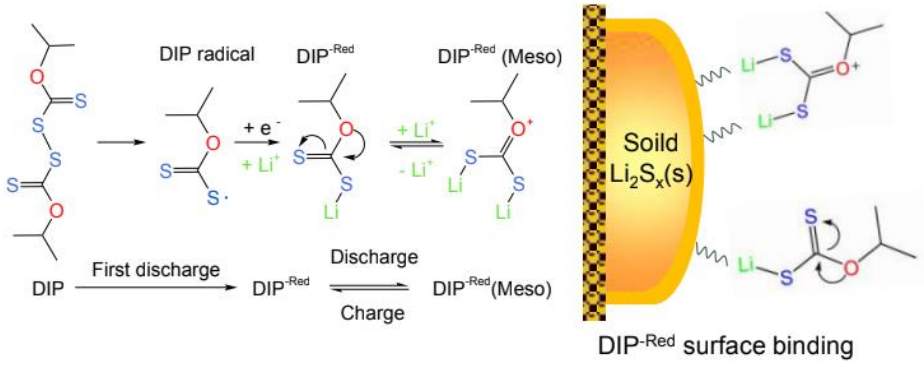

Figure 4.7 Literature-proposed evolution of DIP-derived redox mediator species and their interaction with solid lithium polysulfides. DIP undergoes reductive activation to form DIP-Red and DIP-Red (Meso) species, which were proposed to interact with solid Li_2S_x and mediate sulfur conversion. Adapted from Zhang et al. (2026).

The mechanism shown in Figure 4.7 was developed for a weakly solvating FPDS/G2 electrolyte involving quasi-solid-state sulfur conversion and solid Li_2S_x. In contrast, the present work used DIP-Red prepared separately with Li_2S and subsequently introduced into an electrolyte containing dissolved polysulfides. The literature mechanism therefore provides evidence for the redox activity and polysulfide interaction of DIP-derived species but should not be interpreted as a direct description of the molecular pathway in the present system.

Based on the combined observations, DIP-Red is proposed to influence sulfur evolution primarily after nucleation. Sulfur generation remained centered on the Pt wire, while the presence of DIP-Red was associated with continued droplet growth, displacement from

the electrode, detachment, and redistribution into the surrounding electrolyte. The exact molecular process responsible for this behavior remains to be determined.

Overall, LiI and DIP-Red produced distinct sulfur-evolution behaviors. LiI extended the sulfur-generation region through an iodine-mediated pathway, whereas DIP-Red primarily affected the growth, detachment, and transport of droplets after sulfur had formed on the Pt wire. The observed detachment behavior demonstrates that DIP-Red was effective in modifying the post-nucleation evolution of supercooled liquid sulfur, although further electrochemical and spectroscopic measurements are required to establish the underlying molecular mechanism.

4.5 Summary

In this chapter, the influence of DIP-Red on sulfur evolution was systematically investigated using the customized in situ optical electrochemical cell. An optimized DIP-Red preparation procedure was first established by evaluating different solvent systems, DIP concentrations, and DIP – to – Li_2S ratios. A stable 0.2 M DIP solution with a 1:1.2 DIP – to – Li_2S molar ratio was selected for subsequent experiments because it provided good solution stability while minimizing the formation of insoluble by-products.

Real-time optical observations showed that sulfur droplets in the DIP-Red electrolyte initially nucleated on the Pt wire, similar to the baseline electrolyte. However, unlike the LiTFSI system, the sulfur droplets were more readily displaced from the electrode surface during continued charging, detached into the surrounding electrolyte, and eventually settled within the observation chamber. These observations indicate that DIP-Red primarily influences the evolution and transport of sulfur droplets after nucleation rather than changing the initial sulfur-generation location.

Raman spectroscopy confirmed the formation of elemental sulfur in the optically observed droplets and in the reaction-derived sulfur product. Together with the optical observations, these results indicate that DIP-Red modifies sulfur-droplet evolution after nucleation. However, because quantitative electrochemical comparison was not included in this study, conclusions regarding reaction kinetics, oxidation overpotential, or total sulfur conversion cannot be drawn from the present results. Unlike LiI, which promotes sulfur generation throughout the electrolyte through an iodine-mediated sulfur-conversion pathway, DIP-Red regulates sulfur evolution mainly by facilitating droplet growth, detachment, and transport after sulfur nucleation. These findings demonstrate that different redox-active electrolyte additives regulate supercooled liquid sulfur formation through distinct mechanisms and provide additional insight into the dynamic sulfur-conversion processes in lithium–sulfur batteries.

CHAPTER FIVE

CONCLUSION AND FUTURE WORK

5.1 Conclusions

This thesis investigated the formation and evolution of supercooled liquid sulfur in lithium–sulfur batteries using a customized in situ optical electrochemical cell. By combining real-time optical visualization, Raman characterization, and qualitative reaction-mixture observations, the effects of two redox-active electrolyte additives, LiI and DIP, on sulfur conversion were systematically investigated.

The first objective of this work was to understand the influence of LiI on sulfur evolution. The optical observations showed that LiI fundamentally changed the sulfur-generation behavior during charging. Compared with the LiTFSI electrolyte, sulfur generation in the LiI electrolyte extended from the Pt wire into the surrounding electrolyte. Increasing the LiI concentration resulted in broader sulfur distribution, larger sulfur droplets, and increased sulfur coverage.

The second objective was to investigate the effect of DIP-Red on sulfur evolution. An optimized DIP-Red preparation procedure was established by selecting a stable DIP – to – Li_2S composition and using the supernatant for subsequent experiments. Unlike LiI, sulfur droplets in the DIP-Red electrolyte continued to nucleate on the Pt wire but detached more readily from the electrode surface and migrated into the electrolyte. Raman characterization confirmed that the observed droplets contained elemental sulfur, while optical observations showed that DIP-Red influenced droplet growth, detachment,

and redistribution after nucleation. Overall, the results demonstrate that different redox-active electrolyte additives regulate supercooled liquid sulfur formation through distinct behaviors. LiI promotes sulfur generation by introducing an iodine-mediated sulfur-conversion pathway, whereas DIP-Red primarily modifies post-nucleation droplet evolution, including droplet growth, detachment, and redistribution. These findings provide new insight into sulfur-conversion mechanisms and demonstrate the capability of in situ optical electrochemical techniques for directly visualizing dynamic sulfur evolution in lithium–sulfur batteries.

5.2 Future Work

Building upon the findings of this thesis, several research directions are currently being pursued to further understand and regulate supercooled liquid sulfur formation.

The first direction is the investigation of different carbon host materials. While this work employed a Pt-wire working electrode to directly visualize sulfur evolution, practical lithium–sulfur batteries utilize porous carbon hosts with complex surface structures. Future studies will investigate sulfur evolution on different carbon materials, including carbon fibers and other conductive carbon architectures, to understand how surface morphology influences sulfur nucleation, droplet growth, and transport.

The second direction is the development of advanced electrolyte systems. In addition to LiI and DIP, other redox-active additives and solvent systems will be explored to further regulate sulfur conversion. Comparing different electrolyte formulations may provide new strategies for stabilizing supercooled liquid sulfur and improving sulfur utilization.

The third direction is the investigation of sulfur evolution under fast-charging conditions. Preliminary observations indicate that sulfur evolution behavior changes significantly

under high charging rates. Future work will examine the influence of current density and charging protocol on sulfur nucleation, droplet evolution, and sulfur redistribution using the customized in situ optical electrochemical platform.

Finally, future work will focus on improving the quantitative characterization of sulfur evolution. Additional experiments under identical electrochemical and optical conditions will be conducted to evaluate the effects of electrolyte composition, applied potential, and charging time on sulfur nucleation, droplet growth, surface coverage, and spatial distribution. Because conventional optical microscopy records only a selected focal plane, complementary imaging and spectroscopic techniques will also be explored to better understand droplet evolution at different depths within the electrolyte. Combining these measurements with electrochemical data will provide a more complete understanding of sulfur-conversion dynamics.

Overall, the customized in situ optical electrochemical platform established in this work provides a versatile experimental tool for investigating sulfur-conversion mechanisms. More importantly, the ability to directly visualize sulfur evolution in real time provides new opportunities for understanding dynamic electrochemical processes that cannot be resolved using conventional ex situ characterization techniques.

REFERENCES

Gerber, L. C. H., Frischmann, P. D., Fan, F. Y., Doris, S. E., Qu, X., Scheuermann, A. M., Persson, K. A., Chiang, Y.-M., & Helms, B. A. (2016). Three-dimensional growth of Li_2S in lithium–sulfur batteries promoted by a redox mediator. Nano Letters, 16(1), 549–554. https://doi.org/10.1021/acs.nanolett.5b04189

Goodenough, J. B., & Park, K.-S. (2013). The Li-ion rechargeable battery: A perspective. Journal of the American Chemical Society, 135(4), 1167–1176. https://doi.org/10.1021/ja3091438

Liang, X., Hart, C., Pang, Q., Garsuch, A., Weiss, T., & Nazar, L. F. (2015). A highly efficient polysulfide mediator for lithium–sulfur batteries. Nature Communications, 6, 5682. https://doi.org/10.1038/ncomms6682

Liu, N., Zhou, G., Yang, A., Yu, X., Shi, F., Sun, J., Zhang, J., Liu, B., Wu, C.-L., Tao, X., Sun, Y., Cui, Y., & Chu, S. (2019). Direct electrochemical generation of supercooled sulfur microdroplets well below their melting temperature. Proceedings of the National Academy of Sciences of the United States of America, 116(3), 765–770. https://doi.org/10.1073/pnas.1817286116

Manthiram, A. (2020). A reflection on lithium-ion battery cathode chemistry. Nature Communications, 11, 1550. https://doi.org/10.1038/s41467-020-15355-0

Manthiram, A., Fu, Y., Chung, S.-H., Zu, C., & Su, Y.-S. (2014). Rechargeable lithium–sulfur batteries. Chemical Reviews, 114(23), 11751–11787. https://doi.org/10.1021/cr500062v

Pang, Q., Liang, X., Kwok, C. Y., & Nazar, L. F. (2016). Advances in lithium–sulfur batteries based on multifunctional cathodes and electrolytes. Nature Energy, 1, 16132. https://doi.org/10.1038/nenergy.2016.132

Seh, Z. W., Sun, Y., Zhang, Q., & Cui, Y. (2016). Designing high-energy lithium–sulfur batteries. Chemical Society Reviews, 45(20), 5605–5634. https://doi.org/10.1039/C5CS00410A

Shi, F., Guo, X., Chen, C., Zhuang, L., Yu, J., Qi, Q., Zhu, Y., Xu, Z.-L., & Lau, S. P. (2023). Unlocking liquid sulfur chemistry for fast-charging lithium–sulfur batteries. Nano Letters, 23(17), 7906–7913. https://doi.org/10.1021/acs.nanolett.3c01633

Subramaniam-Venkatesh, P., Gao, Z., Hao, H., Xie, X., Karrar, T., Xia, Z., Spielman-Sun, E., Wang, X., Zheng, X., & Yang, A. (2025). Chemically generated liquid sulfur droplets at room and subzero temperatures. ACS Nano, 19(32), 29682–29690. https://doi.org/10.1021/acsnano.5c09160

Whittingham, M. S. (2012). History, evolution, and future status of energy storage. Proceedings of the IEEE, 100, 1518–1534. https://doi.org/10.1109/JPROC.2012.2190170

Xiong, S., Regula, M., Wang, D., & Song, J. (2018). Toward better lithium–sulfur batteries: Functional non-aqueous liquid electrolytes. *Electrochemical Energy Reviews, 1*(3), 388–402. https://doi.org/10.1007/s41918-018-0015-y

Zhang, X., Wang, Y., Cheng, X., Tian, F., An, Y., Luo, X., Xu, C., Lu, Y., Feng, Y., & Liu, Y. (2026). Synergistic electrolyte solvation and mediation engineering for quasi-solid-state sulfur electrochemistry [Manuscript submitted for publication].